1 **An Earth Observation Land Data Assimilation System (EO-LDAS)**

2

3 P. Lewis*[1], J. Gomez-Dans[1], T. Kaminski[2], J. Settle[3], T. Quaife[4], N. Gobron[5], J. Styles[6], M. Berger[7]

4

5 1. Department of Geography, UCL, and National Centre for Earth Observation, Gower St., London,

6 WC1E 6BT, UK.

7 2. FastOpt, Lerchenstr. 28a, D-20767 Hamburg, Germany.

8 3. National Centre for Earth Observation, University of Reading, Reading RG6 6AL, UK

9 4. College of Life and Environmental Sciences, University of Exeter and National Centre for Earth

10 Observation, Peter Lanyon Building, Penryn, Cornwall, TR10 9EZ, UK.

11 5. European Commission, DG Joint Research Centre, Institute for Environment and Sustainability,

12 Global Environment Monitoring Unit, TP 272, via Enrico Fermi 2749, I-21027 Ispra (VA), Italy.

13 6. Assimila Ltd., 1 Earley Gate, Reading RG6 6AT, UK.

14 7. ESA ESRIN, Science Strategy, Coordination and Planning Office (EOP-SA), Via Galileo Galilei,

15 Casella Postale 64, 00044 Frascati (RM), Italy.

16

19

20 **Abstract**

21 Current methods for estimating vegetation parameters are generally sub-optimal in the way they

22 exploit information and do not generally track uncertainties. We look forward in the future to

23 operational data assimilation schemes to track land surface processes and exploit multiple types of

24 observation. Data assimilation schemes seek to combine observations and models in a statistically

25 optimal way taking into account uncertainty in both, but have not yet been much exploited in this

26 area. The EO-LDAS scheme and prototype, developed under ESA funding is designed to exploit the

27 anticipated wealth of data that will be available under GMES missions such as the Sentinel family

28 of satellites to provide improved mapping of land surface biophysical parameters. This paper

29 describes the EO-LDAS implementation, and explores some of its core functionality. EO-LDAS is a

30 weak constraint variational data assimilation system. The prototype provides a mechanism for

31 constraint based on a prior estimate of the state vector, a linear dynamic model, and Earth

32 Observation data (top of canopy reflectance here). The observation operator is a non-linear optical

33 radiative transfer model for a vegetation canopy with a soil lower boundary, operating over the

34 range 400 to 2500 nm. Adjoint codes for all model and operator components are provided in the

35 prototype by automatic differentiation of the computer codes.

36

37 In this paper, EO-LDAS is applied to the problem of estimating a subset of six of the parameters

38 controlling the radiative transfer operator over the course of a year (> 2000 state vector elements).

39 Zero and first order process model constraints are implemented and explored as the dynamic model.

40 The assimilation estimates all state vector elements simultaneously. This is performed in the context

41 of a typical Sentinel-2 MSI operating scenario, using synthetic MSI observations simulated with the

42 observation operator, with uncertainties typical of those achieved by optical sensors supposed for

43 the data.

44

45 The experiments consider a baseline state vector estimation case where dynamic constraints are

46 applied, and assess the impact of dynamic constraints on the *a posteriori* uncertainties. The results

47 demonstrate that reductions in uncertainty by a factor of up to two might be obtained by applying

48 the sorts of dynamic constraints used here. The hyperparameter (dynamic model uncertainty)

49 required to control the assimilation are estimated by a cross-validation exercise. The result of the

50 assimilation is seen to be robust to missing observations with quite large data gaps.

51

1 Introduction

1.1 Background

One of the primary goals of Earth Observation (EO) is to provide objective and reliable information on the current and (particularly within the satellite EO era) historical state and dynamics of the Earth environment. A major component of this that has been a significant focus of research efforts on monitoring terrestrial vegetation, but EO data are usually of a radiometric nature and do not give direct estimates of the properties of the Earth land surface that we wish to map. Some level of *inference* is therefore needed.

Early studies in terrestrial vegetation monitoring from EO (Richardson and Wiegand, 1977; Tucker, 1979) found that simple transformations of multispectral measurements at red and near infrared wavelengths gave a signal that was responsive to the relative amount of green biomass and that could be used to track vegetation dynamics (Goward et al., 1985). The attractions of such 'Vegetation Indices' (VIs) are obvious: they are visually impressive as spatial and temporal datasets; they are simple to produce and provide a single quantity to interpret; they compensate for some of the extraneous factors that can otherwise complicate lower level EO signals; and they can often provide effective information for time series analyses, where the timing, rather than the magnitude of events is of importance (e.g. vegetation phenology). Further, such indices can be directly targeted at particular functional or physical vegetation properties, such as the fraction of absorbed photosynthetically active radiation (fAPAR) or Leaf Area Index (LAI), by design (Gobron et al., 2002, 2010) or empirically (Rochdi and Fernandes, 2010). In the former case a calibration is achieved using a set of radiative transfer model runs over a range of conditions (Gobron et al., 2000). In the latter, extensive ground-based measurements must be made (Chen et al., 2002) and the form of the relationship with a particular VI assumed. Such efforts are fast to process and often effective, especially for near-real-time survey. They have a range of known failings (Baret and Guyot, 1991), but some of these, such as dependence on the angular conditions of data acquisition

78 can be reduced by treating the data to normalise for such effects (e.g. Rochdi and Fernandes, 2010).

79 Ultimately though, however much care is taken to treat such effects, methods assuming such fixed

80 mappings from VIs with 'statistical' models are open to many criticisms, some of the more

81 significant of which could be considered: (i) they fail to make full use of the information content of

82 the observational data; (ii) they (often) fail to make use of our understanding of the physics of the

83 situation; (iii) they need recalibration if conditions change (e.g. sensor band pass functions or scale

84 of observation); (iv) they tend not to treat uncertainty in the mapped product in any rigorous way

85 (mostly, they fail to consider this at all).This is a judgement call.

86

87 An alternative stratagem has been to build mathematical models of the physics of radiation

88 interactions with vegetation canopies and the intervening atmosphere, phrased as functions of

89 'control' variables (polarisation, wavebands, viewing and illumination angles etc.) and (bio) physical

90 parameters or 'state variables' (LAI, leaf chlorophyll concentration etc. for the canopy, and aerosol

91 optical depth, ozone concentration etc. for the atmosphere), and to use these to attempt to interpret

92 the satellite signal. We may call these radiative transfer (RT) models. To tie in with discussions

93 below and to provide consistency with the data assimilation literature, such models are called here

94 'observation operators' (denoted $H(x)$) in that they map from the state variable vector x to the EO

95 signal (as a vector) R for a given set of control variables, so the modelled signal vector $R = H(x)$.

96 The 'remote sensing inverse problem' then is to obtain an estimate of some function of x, $F(x)$

97 from measurements R. How this may be achieved is discussed in more detail below.

98

99 Much effort has been devoted to producing information from EO data about specific biophysical

100 quantities that are relevant to science and society. A major focus of this has been to attempt to

101 provide estimates of (green) LAI. Garrigues et al. (2008) consider four representative EO-derived

102 global LAI products, with core spatial resolutions of 1 km or coarser, that use what might be

103   considered state of the art methods for multi-year dataset generation. The reader is referred to that

104   paper for detailed information on the products, a product inter-comparison and validation against

105   independent ground measurements. The temporal resolution of the products varies from 8 days to 1

106   month. Three of the products (ECOCLIMAP, GLOBCARBON (V1), and CCRS) are derived from

107   assumed VI relationships with LAI. A fourth (MODIS (C4)) uses such a relationship for a backup

108   algorithm. Three of the products (GLOBCARBON, CYCLOPES (V3.1) and MODIS) make use of

109   RT models in attempting to estimate the LAI. In the case of GLOBCARBON the RT model is used

110   to calibrate the VI-LAI relationship. For MODIS a look up table derived from the RT model is used

111   to map red and near infrared (NIR) bidirectional reflectance data to LAI, and for CYCLOPES a

112   neural network derived from an RT model is used for the mapping from red, NIR and shortwave

113   infrared (SWIR) portions of the electromagnetic spectrum. A feature of these uses of RT models is

114   that they can map many channels of input data to one (or many) outputs. The one-to-one mapping

115   used in VI design and/or calibration is then just the simplest case of this more general RT approach.

116

117   A major new effort in satellite data provision is the GMES (Global Monitoring for Environment and

118   Security; www.gmes.info) programme (Council of the European Union, 2010). It is an EU initiative

119   set up to provide timely information on key environmental variables for policy makers and public

120   authorities, and is intended to be a major EU contribution to understanding and managing climate

121   change. Six thematic areas are being developed: marine, land, atmosphere, emergency and security

122   and climate change. The land monitoring service is provided via the GEOLAND2 project

123   (www.gmes-geoland.info), which oversees the generation of products derived from satellite data,

124   providing information on a wide range of variables including LAI. GMES is a European

125   contribution to GEOSS, the Global Earth Observing System of Systems (European Commission,

126   n.d.). The Sentinels are a series of satellites being developed by the European Space Agency that are

127   specifically designed to address the space observation requirements of GMES. There are five

128   Sentinel missions, each of which will consist of a pair of satellites (for details see Aschbacher et al.,

2012 and dedicated Sentinel mission papers, all this RSE issue). This paper is primarily concerned with methods for the retrieval of biophysical parameters of terrestrial ecosystems, including LAI, from instruments at arbitrary spatial resolutions, sun-sensor geometries and optical wavelengths. Consequently the techniques described here are directly relevant to Sentinels 2 and 3 missions. Sentinel 2 has a medium resolution multispectral imager (MSI) in the optical domain with 4 bands at a 10m resolution, 6 bands at 20m and 3 bands at 60m. These 13 spectral channels (Table 1) are distributed in the visible and near infrared and shortwave infrared regions. The Ocean Land Color Instrument (OLCI) instrument on board the Sentinel 3 platform is a coarser (circa 500m) resolution instrument, similar to MERIS that is designed for global monitoring applications. In principle the system described in this paper could also be extended to other wavelength domains and consequently be used to integrate data from the entire suite of EO missions.

TABLE 1 ABOUT HERE

An additional context for this paper is the growing interest in the application of wider constellations of satellites for environmental and disaster monitoring. A manifestation of this is the NASA A-train (NASA, 2010), which is a formation of complementary satellites and sensors taking observations at close to the same time. Other examples include relatively low cost satellites and instruments with a suite of similar instruments flying in formation to provide global daily viewing opportunities at mid-resolution (10-30m), for example the Disaster Monitoring Constellation (DMC) (DMCII, 2010). The concept can potentially be applied to more heterogeneous systems, such as the 'virtual constellation' for Land Surface Imaging (LSI) concept promoted by the Committee on Earth Observation Satellites (CEOS) to optimise benefits from land remote sensing systems (CEOS, 2011a). There are clear benefits for monitoring frequency if data from a wider range of sensors are available, but the more heterogeneous the set of sensors (in terms of spatial resolution and wavelength domains) the more important it is to formalize appropriate methods to optimally merge

155   information from these sources.

156

157   **1.2 Optimal estimation**

158   The remote sensing inverse problem described above can be phrased as an optimal estimation

159   problem, requiring an estimate of a distribution around the minimum of some function of an

160   observation residual vector, such as an ℓ^2-norm. Our assimilation system is based on the joint

161   inversion approach of (Tarantola, 2005) and is most conveniently formulated in what is often called

162   a Bayesian context (Enting, 2002), which means that each piece of information (including any prior

163   information on the state variables) is represented by a probability density function (PDF).

164   Combining this information yields an *a posteriori* PDF for the parameters, which is the

165   result/solution of the assimilation problem. If all of these PDFs are Gaussian and the models

166   involved not too non-linear (potentially after a transformation) then the posterior parameter PDF

167   can also be approximated by a Gaussian:

168

169   $\rho(x) = \exp\left(-J(x)\right)$

170

171   which is the maximum likelihood estimate of the state variables *x*, thus the minimum of a cost

172   function which takes the form:

173

174   $J\left(x\right) = \sum_i J_i\left(x\right)$ (1)

175

176   where $J_i\left(x\right)$ is a cost function expressing a constraint *i*, a member of some set of constraints.

177

178   Much of the earlier literature on estimating *x* for vegetation monitoring from a physical basis

179   concentrated on exploring options in numerical minimisation approaches (see e.g. the review by

180   Kimes et al. (2000)) based almost entirely on using a single cost function $J_{obs}(x)$ expressing a

181   mismatch between EO data and the prediction of an observation operator $H(x)$ (a radiative transfer

182   model). The optimisation methods explored include, but are not limited to, downhill simplex

183   (Privette et al., 1994), gradient methods (Gill et al., 1981; Liang and Strahler, 2002), neural

184   networks, look-up tables and genetic algorithms (GA) (Combal et al., 2003; Myneni et al., 1995;

185   Weiss et al., 2000). Although appropriate optimisation strategies and computer implementations

186   have been around for some time that make use of J'_{obs}, the gradient of J_{obs} with respect to x, in

187   locating the minimum, they have not been widely used in terrestrial EO monitoring, primarily

188   because of the perceived computational cost and numerical issues if finite difference methods are

189   used to estimate J'_{obs}, and more particularly because it is no trivial job to differentiate radiative

190   transfer models. The advent of automatic differentiation (AD) methods and tools such as TAF (e.g.

191   Giering and Kaminski, 1998, Lavergne et al., 2007б) or TAPENADE (e.g. Qin et al., 2007) means

192   that calculating J'_{obs} for radiative transfer or other models is now quite feasible at computational

193   costs not greatly dissimilar to the calculation of J_{obs}. The approach has first been applied to rather

194   simple RT models such as RPV (Lavergne et al., 2007) and a two-stream model (Pinty et al., 2007;

195   Clerici et al., 2010), but this is equally appropriate for more complex models as we show here. The

196   ability to make rapid, exact calculation of the gradient vector not only widens the choice of

197   algorithms that might be used to minimise the cost function, but also provides a route for potentially

198   faster state vector estimation, and perhaps most importantly allows larger dimensioned problems to

199   be tackled. Qin et al. (2008) were perhaps the first to apply AD to more complex RT models

200   (MCRM of Kuusk (1995)) using a combination of GA and a cost function-based method using J'_{obs}

201   in the region of a trust region derived from the GA. In this case 7 members of the (dimension 14)

202   state vector are estimated, but only at a single point in time. Results are not shown for parameters

203   other than LAI, and no detailed consideration of uncertainty is included, but the ability to use AD in

204   such scenarios is clearly demonstrated.

205

Data producers and users generally have little influence over control variables to the estimation problem, as satellite sensors and missions are usually designed to serve (or are used to serve) multiple purposes, and involve compromises in sensor design and orbits. Any one sensor (and the resultant set of control variables entailed) then will tend to be sub-optimal for a task as specific as vegetation monitoring. Inevitably this results in individual EO data sources having information content that is too low to provide accurate retrievals of the entire state vector space. Some parameters may never be completely retrievable on the basis of observation alone, especially where there is equifinality between two or more parameters over the domain of the observed data, that is, when the same model state can be reached by different combinations of state variables. See for example (Beven, 2006) for an overview of this issue or Lewis and Disney (2007) for an attempt at explaining mechanisms impacting this in canopy radiative transfer. The core of the issue is that the observations only refer to a subspace of the unknown state variable space. In this case, no information on some directions in state space can be gained from the observations, and their values will have to be constrained using for example, prior information. Such problems are described as being ill-posed. As an example, consider the often-desired goal of tracking the temporal evolution of some parameter of interest such as LAI, to provide information on phenology. Inverting a model on a daily basis where there may only be a small number of observations, or none at all, is typically not possible as a single observation does not have enough information to constrain all of the state vectors of typical radiative transfer models. This has been solved implicitly in the production of many current EO data products by assuming the model parameters to be constant over some time interval, and many of the ancillary parameters such as those governing leaf and soil properties are simply assumed known (and fixed as is the case when using VIs). Assumptions such as temporal invariance or knowledge of ancillary variables are pragmatic responses to the remote sensing problem being ill-posed, but it is better if possible to seek less *ad* hoc methods for constraining our estimate, especially if we wish to estimate uncertainty in the product.

232   A mechanism that provides scope for dealing with such problems is the suite of tools that are

233   collectively referred to as 'Data Assimilation' (DA). There is no strict definition as to what

234   constitutes DA but it is taken here to mean the statistically optimal merging of data and models.

235   Optimality, in this sense, implies the need to take into account uncertainties in all parts of the

236   system.

237

238   **1.3 Data Assimilation**

239   Data assimilation can be seen as mechanism for combining models and data. The defining feature of

240   DA, at least by the definition provided in this paper, is that it enables the use of additional

241   assumptions to make parameter estimation viable in situations that exhibit ill-posedness. In essence,

242   we have a mechanism through equation 1 to combine multiple constraints. An example of this that

243   has long been used either explicitly or implicitly in the inference of land surface parameters from

244   EO is constraint via *a priori* estimates of parameter values or ranges (or more generally,

245   distributions). What DA specifically brings to bear on the problem is a dynamic model of parameter

246   evolution in space and/or time.

247

248   Early examples of data assimilation systems are those used to improve short-range weather

249   predictions from meteorological models (Ghil and Malanotte-Rizzoli, 1991). In these systems the

250   number of state variables is typically huge, often greater than 10^6, because of the large number of

251   interconnected sub-domains used to represent the atmosphere in a 3D grid. The number of

252   observations available is typically several orders of magnitude less than this, and in consequence

253   the problem is ill-posed. However, including a constraint that the final solution should not diverge

254   too far from an *a priori* estimate (typically supplied by a previous model run) tends to result in a

255   tractable solution. The schemes used for these problems are referred to as 'variational', being based

256   in the field of mathematics dealing with the calculus of variations, and are closely related to the DA

257   system described in this paper. A 'strong constraint' variational DA system assumes that the

underlying process model prescribing the state vector evolution is correct (i.e. there is a model trajectory that matches the observations). In this case it is generally only the initial state of the system that is estimated by the DA procedure, but this approach can also be used to calibrate models (i.e., to optimise estimates of model process parameters) (Knorr et al., 2010). If the state vector is allowed to deviate from the model predictions then this is referred to as a 'weak constraint' DA system (Zupanski, 1997). It is this latter type that is used here and is discussed more completely in later sections.

We note that these systems have been exploited to estimate LAI from MODIS data by making use of a coupled phenology temporal trajectory model with a radiative transfer model (Xiao et al. 2009; Xiao et al. 2011). MODIS LAI is assimilated into a crop model using a variational technique in Fang et al. (2008a). The variational approach is shown to help in retrieving surface fluxes in Olioso et al. (2005) and Qin et al. (2007), and has found wide application in the hydrological literature (see for example McLaughlin, (2002)).

Another related set of techniques in the DA canon may be called sequential methods. The most widely-known and widely-used example of these is the Kalman Filter. Sequential methods generally only consider observations at a single time step and adjust the model state vector at that time by an amount proportional to the differences between the observations and the predictions of those observations using that model state. Using a variant of the Kalman Filter, known as the Ensemble Kalman Filter (Evensen, 2003), Quaife et al. (2008) demonstrated the assimilation of satellite reflectance data into a simple ecosystem model using an RT model as observation operator. Other efforts have used these techniques to assimilate e.g. snow data (Slater and Clark, 2009) or MODIS-derived LAI into a phenology model (Stöckli et al., 2008). The related technique of particle filtering has been used to assimilate microwave temperature in order to infer soil moisture dynamics in Qin et al. (2009).

284

The Earth Observation Land Data Assimilation System (EO-LDAS) study funded by ESA aims at supporting the generation of a generic land data assimilation system by using the full information content provided by observations from satellite constellations. Such a system, in eventual operational form, is intended primarily to improve the quality and consistency of land surface products generated from multi-sensor EO data. The project is focussed on developing a generic scheme and software prototyping for use with medium to mid spatial resolution (in the range 10m – 500m) optical data. The principal design concept is to allow integration of data from different satellites observing the surface of the earth at different sun-sensor geometries, wavebands and spatial scales, such as that supplied by Sentinels 2 and 3, in a physically consistent manner, and to provide information on the state of the surfaces with well-quantified estimates of uncertainty. It also demonstrates the idea that predictions based on data from one sensor can be made from a DA system driven by observations from another, a concept that could potentially be used to aid vicarious sensor calibration.

2 The EO-LDAS prototype

2.1 The EO-LDAS Scheme

The EO-LDAS prototype is an initial version of the scheme, designed to carry out a core set of DA functions. In particular, in the *scheme*, it performs an atmospheric correction of images to top-of-canopy reflectance, retrieves canopy state variables using surface reflectance data and a constraint model and simulates top-of-atmosphere radiance or reflectance for a given surface and atmosphere. This preserves the essential features of a more comprehensive system (incorporating a fuller coupling between the surface and atmosphere), while allowing development and further study of the most important elements - the observation operators and the assimilation techniques.

309

310 To simplify the prototype, we have assumed a large length scale for variations in atmospheric

311 scattering properties, and a very short length scale for surface variability. With these assumptions,

312 we can correct an image (or sub-image) with a single set of atmospheric state variables, use

313 reflectance data in a multi-temporal assimilation on a cell-by-cell-basis, and simulate a top-of-

314 atmosphere radiance field using the same atmosphere for each of a set of model grid cells. This

315 process can be iterated to achieve the surface-atmosphere coupling. To relax either constraint

316 would mean we have to deal with the inversion of a coupled surface-atmosphere problem over a

317 large number of cells, which would require considerable computing resources, both in terms of

318 memory (for the covariance structures involved) and the time needed to carry out the actual

319 inversion, without necessarily improving our ability to monitor the land surface. A tutorial guide

320 explaining the functionality and use of the prototype system is available online[1].

321

322 The DA system can be considered to have two main components: (i) a set of constraints, expressed

323 via equation 1; (ii) an assimilation algorithm, i.e. a way to apply the constraints to achieve the

324 optimal estimate of the state vector. The set of constraints in EO-LDAS involves: (i) an

325 observational constraint $J_{obs}(x)$, requiring data (from EO or ground measurements) and a model for

326 translating from state space to observation space (the observation operator); (ii) a dynamic model

327 constraint $J_{model}(x)$, conditioning the temporal (and/or spatial) evolution of the state vector; (iii)

328 physical or empirical bounds and/or distribution constraints $J_{prior}(x)$ to the state vector elements;

329 Thus, in EO-LDAS, equation 1 becomes:

330

331 $$J(x) = J_{obs}(x) + J_{prior}(x) + J_{model}(x)$$

332

333 Each of these constraints has associated with it an error model. In the following sections, we

---

[1] http://www2.geog.ucl.ac.uk/~plewis/eoldas/

334 describe the set of constraints and the DA algorithm. We stress that in the text below, we use the

335 symbol x to refer to the set of state variables that we wish to estimate. In EO-LDAS this essentially

336 means a representation of the state at each sample points in time (and/or space) that we consider.

337 So, for example if we were trying to estimate Leaf Area Index and leaf Chlorophyll content at one

338 location for every day of the year, we would have a state vector with 361x2 elements. In addition,

339 EO-LDAS has the capacity to augment this state vector with 'static' state representations (some

340 term affecting one or more of the constraints that we wish to be considered constant in space/time).

341

342 **2.2 Observational Constraint**

343 Given the EO context of this system, at least one of these constraints should be based on

344 observations. The cost function is generally weighted for observation and observation operator

345 uncertainty and correlation (assumed in EO-LDAS Gaussian and described by C_{obs}):

346

347 $$J_{obs}(x) = \frac{1}{2}(R - H(x))^T C_{obs}^{-1}(R - H(x))$$ (2)

348

349 where ^{T} denotes the transpose operator. This is the penalisation associated with differences between

350 the predicted and observed reflectance values. The covariance matrix C_{obs} describes the uncertainty

351 in the observations (and also formally, in the observation operator). As noted, the purpose of the

352 observation operator $H(x)$ is to translate information from the state space to that of the

353 observations, and is in practice a radiative transfer model. For ease of implementation (mainly

354 involving spectral sampling issues), when different sensor types are used in EO-LDAS, a set of

355 $J_{obs}(x)$ terms is developed, with one for each sensor type.

356

357 There have been many attempts to create observation operators $H(x)$, varying in complexity,

358 accuracy and computational cost. Goel (1988) provides a review of most of the concepts for

radiative transfer model developed for reflectance from vegetation canopies at optical wavelengths (see also (Goel and Thompson, 2000), with (Tha Paw U, 1992) covering related materials for thermal emitted radiation and (Fung and Chen, 2010) for the microwave domain. Some updates and model intercomparisons are provided by Sobrino et al. (2005) (thermal) and Widlowski et al., (2007) (optical). The focus in this paper, and in the prototype EO-LDAS is on the use of optical sensor data, but the approach outlined here is easily adapted for use in other wavelength domains.

In a similar way, atmospheric properties, such as aerosol optical depth and water vapour content, need to be accounted to obtain accurate estimates of surface properties. This can be achieved by coupling the surface model with an atmospheric model, and solving for both the surface and atmosphere parameters simultaneously (Verhoef and Bach, 2003). Some (probably most) approaches to surface interpretation use surface reflectance that has already been 'corrected' for atmospheric effects (Vermote et al., 2002), but a full decoupling of the problem, at optical wavelengths at least, cannot be achieved without knowledge of the surface Bidirectional Reflectance Distribution Function (BRDF) (Lyapustin and Knyazikhin, 2001; Lyapustin et al. 2006) (or at least a normalised form of this) (Vermote et al., 1997).

The observation operator we use in this paper is developed from the original semi-discrete model of Gobron et al., (1997). It has a state vector describing canopy architecture and three spectral terms, although these are all defined as functions of other parameters as described below (Table 2). The soil reflectance is assumed Lambertian in the model, although it could be adapted to incorporate a soil directional reflectance model. As stated here then, the (canopy-soil) model estimates the directional reflectance factor at a set of viewing and illumination angles for a given narrow waveband. Since the model must be capable of predicting the reflectance at arbitrary (solar reflective) wavelengths, spectral models are incorporated in the code to predict the soil (Lambertian) reflectance and leaf (bi-Lambertian) reflectance and transmittance. Since model

385   derivatives are required, we use for simplicity here: (i) the linear soil reflectance model of Price

386   (1990); and (ii) an approximation to the PROSPECT leaf reflectance/transmittance model of (Féret

387   et al., 2008), being a minor modification of the model of (Jacquemoud and Baret, 1990). The

388   approximation was developed for possible processing speed enhancements, but is identical in form

389   to PROSPECT if the parameter N (table 2) is 1, and very close to the original model over the range

390   of N 0.8 to 2.5.

391

392   The soil spectral model of Price (1990) characterises a given soil at field capacity as a linear

393   combination of Empirical Orthogonal Functions (EOFs) based on a database of moist (field

394   capacity) soil spectra. Four EOFs are found to account for 99.6% of the cumulative variance of all

395   the soils considered, so, as is usual, we use up to four terms in this implementation. Parameter

396   ranges in Table 2 come from (Price, 1990), figures 11-13.

397

398   TABLE 2 ABOUT HERE

399   TABLE 3 ABOUT HERE

400

401   The leaf angle distribution is categorised in the model of Gobron et al., (1997) and so not set by the

402   assimilation procedure (i.e. it must be pre-defined or the different categories assessed separately:

403   this could ultimately be improved using a continuous description). The assimilation scheme can

404   provide estimates of the remaining (12) state variables for each time period modelled. Following

405   (Weiss et al., 2000) we apply approximate linearization functions to some of the terms (Table 3).

406   The reasons this is appropriate here are: (i) they better condition the problem for optimisation; (ii)

407   the assumptions of Gaussian distributions of errors are more appropriate in this case.

408

409   Differentiated versions of the observational cost are required to enable the use of efficient gradient

410   descent minimisation routines, so we can benefit from access to $J'_{obs}(x)$, the derivative of $J_{obs}(x)$

411   with respect to x. This is:

412

413    $$J_{obs}^{\wp}(x) = -H\wp(x)^T C_{obs}^{-1}(R - H(x))$$ (3)

414

415   where $H\wp(x)$ is the derivative of $H(x)$ with respect to x. An adjoint code of the cost function for

416   the semi-discrete model, i.e. code for direct calculation of $J_{obs}^{\wp}(x)$ that avoids the need for explicit

417   calculation and storage of $H\wp(x)$, was generated from the source code of the model by the

418   automatic differentiation tool TAF (Giering and Kaminski, 1998). The adjoint code implements the

419   chain rule of differentiation in the so-called reverse mode. It provides the gradient information that

420   is accurate up to machine precision at a computational cost that is not greatly dependent of the

421   length of the gradient vector and well below that of the multiple runs of the semi-discrete model

422   that would be required for a finite difference estimate.

423

424   We obtain an estimate of the posterior uncertainty through consideration of the curvature at the

425   global minimum in state space. This is provided by the inverse of the sum of the constraint

426   Hessians, the Hessian for this constraint being $J_{obs}^{\wp\wp}(x)$:

427

428    $$J_{obs}^{\wp\wp}(x) = H\wp(x)^T C_{obs}^{-1} H\wp(x) - H\wp\wp(x)^T C_{obs}^{-1}(R - H(x))$$ (4)

429

430   Although it should be possible to develop a Hessian code in much the same way as done for the first

431   derivative, that has not yet been done within EOLDAS, so a linear approximation to the Hessian is

432   achieved, using finite differences. As we will see below, the algorithm used to perform the

433   optimisation is iterative, but the potentially high cost of using finite differences for the Hessian is

434   unimportant in this sense, as it only has a role in estimating the posterior uncertainties.

435

2.3 Process model constraint

The EO-LDAS prototype is designed to allow the user to interface their own constraints, so long as they provide code to calculate the cost function and its first and second order derivatives. This allows a mechanism whereby (bio)physical process models can be used to constrain the solution and or estimates of the variables controlling those models can be developed. The focus of the prototype software and that of this paper are on understanding how to use DA concepts to improve estimates of biophysical variables from EO data, rather than to test specific process models however. For this reason, we have currently only implemented a linear process model in the system:

$$M(x) = Ax + b \tag{5}$$

where A and b are a matrix and vector respectively. One advantage of designing the prototype system in this manner is that it provides a flexible framework for changing the underlying model. Unlike in a sequential system, this formulation directly allows for any model state vector element to be linked to any other, since x here contains the state representation at all sample times (spaces), so different time/space scales can be readily incorporated. The cost function associated with this process model then is:

$$J_{model}(x) = \frac{1}{2}(x - M(x))^T C_{model}^{-1}(x - M(x)) = \frac{1}{2}((I - A)x - b)^T C_{model}^{-1}((I - A)x - b) \tag{6}$$

where I is the identity operator. $J_{model}(x)$ is the cost incurred by departure of the model state from that predicted by an underlying process model. An interpretation of A is as the model derivative. The model uncertainty matrix C_{model} therefore expresses the uncertainty in this derivative, including any inherent uncertainty in the process model. It such a case, it might often be pragmatic to specify only diagonal terms in C_{model} as further details of model structure are often difficult to obtain. In

461 any case, we can see that EO-LDAS could be interfaced to a process model such as the Carbon Flux

462 model DALEC used by Quaife et al. (2008) or any other for which the derivative might be obtained

463 (e.g. using AD) by augmenting the state vector x by any terms that we might wish to drive the

464 model.

465

466 Whilst the EO-LDAS scheme allows for linking to 'biophysical' or other process models, that is not

467 the main focus of the prototype. Indeed, there are many cases, for instance when conducting a

468 comparison of information derived from EO data and some biophysical model trajectory, when it

469 may be undesirable to directly incorporate a detailed process model. Further, and perhaps more

470 importantly, a fundamental requirement of the EO-LDAS system is that the state vector, x, contains

471 at least the parameters of the observation operator $H(x)$ for every point in time (and/or space), and

472 many of these may not be provided by a biophysical process model designed, for example, to

473 estimate total Carbon fluxes. We should see the matrix A (and if needed, the vector b) then as a

474 much more general interface to 'process modelling' within an optimal estimation environment.

475

476 We can for example consider the benefits of approaches such as Twomey-Tikhonov regularisation

477 or variations around this theme (Rodgers, 2000). Examples of this that we explore further below are

478 first and second order difference constraints. In essence these improve the conditioning of the

479 inverse problem by smoothing or regularising the solution, which comes about because they

480 constrain derivatives (first or second order here) to be zero. In a weak constraint DA system such as

481 that used here, the model is not strictly enforced (this would be clearly undesirable in these

482 derivative constraints) but rather the degree of smoothness in the outcome is traded off against the

483 other factors in $J(x)$ through the model uncertainty matrix. In other words, the cost function will

484 penalise temporal trajectories of parameters that are not flat, but this is 'balanced' with a goodness

485 of fit to the observations and departure from the prior estimate. In practice this constrains the

486 solution toward a smooth evolution by minimising the high frequency components of the temporal

487   parameter trajectory. A similar approach has been taken by Quaife and Lewis (2010) for linear

488   observation operators. Viewing this form of solution as a combination of state variable estimation

489   and filtering, we note that the filter characteristics are controlled by the nature of matrices A and

490   C_{model}, the former controlling the cut-off frequency of the filter and the latter, if simply diagonal,

491   controlling the degree of dampening of the unwanted high frequencies. In this context, we can

492   consider b a bias term, which we set to zero. In this case:

493

494   $$J_{model}(x) = \frac{1}{2}(Dx)^T C_{model}^{-1}(Dx)$$

495

496   where $D = (I - A)$. The derivatives of this are: $J'_{model}(x) = D^T C_{model}^{-1} Dx$ and $J''_{model}(x) = D^T C_{model}^{-1} D$. To

497   achieve Twomey-Tikhonov regularisation then, which we view as an empirical process model, D

498   here becomes simply a (Nth order) differential operator (Quaife and Lewis, 2010). In many

499   situations, we must assume the uncertainty in this empirical constraint unknown. The minimum

500   error model then is a constant value for which we can use a scalar term g:

501

502   $$J_{model}(x) = \frac{g^2}{2} x^T (D^T D) x \qquad (7)$$

503

504   We can interpret g as a 'smoothness term (or g^{-1} as a roughness term) that controls the weighting

505   of the derivative (model) constraint with respect to the other constraints. It is worthwhile at this

506   point trying to relate this back to the discussions on process models. This is most readily achieved

507   by considering a first order derivative constraint. If applied at lag 1 day for a temporal constraint,

508   we can interpret this as an expectation that the state vector tomorrow will be the same as today (i.e.

509   the derivative is zero). If we want to relate this to equivalent sequential methods, we can say that

510   this is a zero-order process model. The term g^{-1} then can be interpreted as uncertainty (phrased as

511 standard deviation) in this model, or alternatively as the growth in uncertainty over a one day

512 period. Similar interpretations apply for other derivative constraints: a second order derivative

513 constraint is equivalent to a first order process model. Equation 5 then is a viable empirical process

514 model constraint, but we have yet to tackle the fact that the smoothness g is unknown. We also note

515 that if we use a scalar for g, we are assuming the same smoothness for all state variables at all times

516 (places).

517

518 An option that arises with dynamic models (where we are making connections between elements of

519 the state vector at different times (places) is what to do about boundary conditions. Even with a

520 simple differential model this needs consideration in forming the D matrix. Among the various

521 options, especially when dealing with annual or multi-annual datasets, an attractive one is to assume

522 periodic boundary conditions, and that is done here. This means that in calculating D at the end of

523 the year (edge of the matrix) we perform the digital differential with state elements from the

524 beginning of the year.

525

526 It is generally found (e.g. Twomey (2002)) that quite a broad range of model uncertainty

527 (smoothness) estimates can provide an acceptable solution, so we do not expect the results to be

528 overly-sensitive to the choice of this 'hyper-parameter'. We could make a rough guess at the model

529 uncertainty, but that is likely to be unsatisfactory in the general case. If we under-estimate it by too

530 much, we can over-dampen most of the state vector. Equally, if we greatly over-estimate the model

531 uncertainty, the impact of the temporal constraints is minimal: in the extreme, an infinite model

532 uncertainty (zero smoothness) leads to a solution without model constraint. Whilst there are several

533 strategies that can be employed to estimate the model uncertainties (hyper-parameters), perhaps the

534 most fruitful in the context of EO-LDAS is running a cross-validation exercise. The idea is that an

535 independent dataset is used to test the robustness of the solution for a particular value of the hyper-

536 parameters. An optimal estimate of the hyper-parameters (or distribution thereof) can be obtained

537   by minimising a cost function with the independent observations. This can be achieved with a sub-

538   set of observations to test a solution obtained from the rest of the dataset, a strategy that when

539   repeated over different subsets becomes known as generalised cross validation becomes known as

540   generalised cross validation (Wahba, 1990, Eilers, 2003 and Lubansky et al., 2006).. Alternatively,

541   we might use data from an independent sensor, although accurate absolute calibration between the

542   sensors is needed for that.

543

544   **2.4 Prior Constraint**

545   An additional constraint mechanism is implemented in EO-LDAS, that we term a prior constraint.

546   Its role, via the cost function $J_{prior}(x)$ is to impose a penalty for deviation from some previously

547   defined state, x_{prior}:

548

549    $$J_{prior}(x) = \frac{1}{2}(x - x_{prior})^T C_{prior}^{-1}(x - x_{prior})$$ (8)

550

551   where C_{prior} expresses the uncertainty of the prior model state, a measure of our belief in the prior

552   estimates, x_{prior}. The derivatives of this cost function are $J'_{prior}(x) = C_{prior}^{-1}(x - x_{prior})$;

553    $J''_{prior}(x) = C_{prior}^{-1}$. A comparison of equations 6 and 8 shows that this is really just another form of

554   model constraint, with $M(x) = x_{prior}$, which can be achieved with the existing model constraint by

555   setting $b = x_{prior}$. In practice, this allows us to enforce a prior belief in the distribution and range of

556   the state vector elements (e.g. a climatology or physical or otherwise know 'reasonable'

557   distributions), although only Gaussian distributions can be considered.

558

559   **2.5 DA algorithm**

560   The various constraints discussed above provide the cost function in equation 1 through their

561 summation. This also applies to the derivatives $J'(x)$ and $J''(x)$. The cost function $J(x)$ is

562 minimised using a gradient descent method (i.e. using $J'(x)$). Bounds are applied as a final

563 constraint to the solution, to ensure that the state vector remains within physical limits. These can be

564 altered by the user for any particular run of the system via a configuration file or command line

565 interface. In the EO-LDAS prototype we use the limited memory Broyden-Fletcher-Goldfarb-

566 Shanno (L-BFGS-B) algorithm described in (Byrd et al., 1995; Zhu et al., 1997). In principle,

567 however, a number of different gradient descent algorithms could be used. The L-BFGS-B was

568 selected for its efficient memory handling for high dimensional problems and the fact that it can

569 optimise over a bounded domain, which is appropriate for this problem.

570

571 The algorithm then is quite straightforward: (i) read in configuration information and observations;

572 (ii) provide an initial estimate of all state vector elements that we wish to estimate; (iii) iterate

573 within the optimisation routine until convergence is reached (or using other criteria) to estimate the

574 state vector; (iv) calculate the Hessian and then its inverse to provide the posterior covariance

575 matrix, the estimate of uncertainty.

576

577 It is instructive to consider the contribution of these three terms in the estimates of Hessian matrix.

578 The observational term can be ill-conditioned if the observations exhibit little sensitivity to some or

579 all of the state variables, for example due to poor combinations of spectral and/or angular sampling.

580 The addition of the prior and dynamic model terms then results in improved conditioning of $J''(x)$,

581 as these extra terms compensate for the lack of observation sensitivity to some of the state variables.

582 They also provide the ability to interpolate (i.e. rely more on the process model) between where we

583 have observations. Importantly, the uncertainties are tracked throughout this process, so when e.g.

584 interpolating over large gaps, we get the expected increase in uncertainty.

585

586 The DA system developed here can be viewed an extension of the methodologies that have been

587 applied to inverting radiative transfer models by minimising a cost function. The addition of a linear

588 dynamic model therefore only adds a handful of extra parameters to the problem (namely, the nature

589 of the dynamic model itself and the associated covariance matrix, C_{model}, which may be simply

590 diagonal). This is in a marked contrast with similar methodologies that either use a long time series

591 of data for inverting one single parameter (in the case of inverting LAI as in (Fang et al. 2008b;

592 Xiao et al. 2009; Xiao et al. 2011). The temporal smoothness constraint is in itself an important

593 feature, which is usually performed as a post-processing step after the parameter retrieval (Lu et al.

594 2007).

595

596 **3. Experimentation**

597 We present a series of experiments to demonstrate the operation of the EO-LDAS prototype and to

598 explore the sorts of capabilities such a system could provide with data from the Sentinel-2 MSI

599 sensor (see table 1a for waveband information for Sentinel-2 MSI). The experiments use synthetic

600 data for observations i.e. are derived from running the observation operator for a given state vector

601 for what we suppose to be typical Sentinel-2 scenarios over one calendar year. We simulate top hat

602 function bandpass functions (1 nm sampling) according to the information in Table 1 (see also

603 Drusch et al., 2012, this issue). The main aim of the experiments is to determine the improvement,

604 in terms of reduced uncertainty, in biophysical parameter estimation that might be obtained by

605 applying the EO-LDAS prototype for such scenarios. A subsidiary aim is to demonstrate the

606 capability of the DA system to make predictions of data from a sensor not used in the DA process.

607 Here, we do this by using the state vector estimates derived from the DA with synthetic MSI data,

608 and make predictions of what a SPOT-5-like instrument would view (described below). These data

609 are used in a cross-validation exercise within the experiments.

610

611 **3.1. Experimental setup**

612 In these experiments, we control the time trajectory of a subset of model parameters according to

613   the functions given in Table 4, where t is the relative day of year (DOY) i.e. DOY normalised by

614   365. All other parameters take their default values given in Table 2. The functions for LAI and

615   chlorophyll broadly mimic typical trajectories of these terms for crops: for LAI, a flat initial period,

616   followed by a rise to maximum LAI and then a symmetric decrease; for Chlorophyll, a linear rise

617   and decrease. The more arbitrary functions used for the soil brightness term s_1 we include to mimic

618   rather broad variations over the year that might be supposed to be responses to soil moisture. A

619   similar function is used here for leaf water, with a time lag of 36.5 days. The quite large variation of

620   these two latter terms is intended primarily to allow the operation of the data assimilation scheme to

621   be explored over a wide range of conditions, rather than to too closely mimic some particular

622   situation. In that context, the rather large time lag between soil brightness variation and leaf water

623   content is unrealistic, but a larger phase between these terms should test the system to a greater

624   extent than having all parameters following similar trajectories. Although the full set of state vector

625   elements is 13 for each time sample, we attempt to retrieve only the 6 elements (no 1, 4, 6, 7, 8, 9 in

626   table 2) (per time sample) that we vary in these experiments, i.e. we assume the remaining elements

627   fixed and known. This is partly to reduce the computational time required for the DA and more

628   broadly because we believe it is sufficient to demonstrate the principles underlying the DA method.

629   It is quite feasible to permit an estimation of 12 of the 13 elements (not the categorical variable

630   directly through this method) but this is not the purpose of this exercise, and (arbitrary) variations in

631   these additional terms would need to be defined to achieve this.

632

633   TABLE 4 ABOUT HERE

634

635   To approximate the Sentinel-2 MSI acquisition geometry (ESA, 2010), we assume one sample

636   every 5 days (73 samples over the year), with a solar zenith angle corresponding to 10:30 local time

637   at 50° N, random relative azimuth and random view zenith between 0° and 15°. Whilst these

638   parameters do not provide a precise prediction of the likely MSI sampling and geometries, they are

close enough to develop an understanding of the likely behaviour of the data. The random azimuth, for example, is clearly in error, but since the view zenith angle is so restricted, this will have very little impact; the local time at 50° N will in reality be slightly later than the nominal equatorial crossing time used here, but the details of the solar zenith angle are less important here than inducing a typical variation over the year (32° to 76° here). The simulation of one sample every 5 days mimics close to the maximum sampling achievable by MSI on 2 Sentinel platforms.

Synthetic observations were also generated for a SPOT5 HRG-like instrument. This sensor has four wavebands (500-590, 610-680, 790-890 and 1530-1750 nm) (CEOS, 2011b). We have assumed a revisit period of 13 days (to be out of sync with the synthetic MSI observations), although the differences are only up to two days from the MSI observations. The view zenith angle was limited to +/-25 degrees from nadir, with a random azimuth and a local overpass time of 10.30. In total, 28 observations were available in this dataset.

Uncorrelated Gaussian noise is added to the observations as part of the data synthesis. We assume the standard deviation of this to vary linearly from 0.008 at the shortest wavelength to 0.020 at the longest, for both the MSI and SPOT-5 HRG. These values are broadly twice those claimed for atmospheric correction of data from the NASA MODIS instrument (Roy et al., 2005). If an atmospheric 'correction' were performed on the data, we would generally expect the uncertainty in surface reflectance to be correlated across wavelengths, as e.g. an under-estimation of aerosol optical thickness would likely give rise to an over-estimate in reflectance for the shorter wavelength bands. Here, we have inflated the assumed (MODIS) uncertainties by a factor of two to take some account of such likely correlation. This highlights one of the benefits of ultimately using a more fully coupled surface-atmosphere observation operator, in that such features would fall naturally out of the model formulation and random noise might be more reasonably assumed for top of atmosphere radiance or reflectance. However, for the purposes of these experiments it is sufficient

665 to treat only the surface (canopy-soil) elements of the observation operator.

666

667 We term this simulation set 'complete' for the purposes of this paper, in that it expresses a rather

668 idealised situation where no clouds are present. A second synthetic observation set that we term

669 'cloudy' (36 observations for MSI and 15 for SPOT-5 HRG) is derived from this, for which we have

670 removed 50% of the observations according to a correlated random function to mimic persistence of

671 cloud cover. This induces ('cloud') data gaps of up to 60 days (mean gap 10.3 days, standard

672 deviation 12.6 days for MSI).

673

674 As noted above, the cost function minimisation is achieved in EO-LDAS with the L-BFGS-B

675 algorithm. A bounded minimisation is performed within this code, with the limits specified on the

676 (transformed) state variables given in Table 2 (transformations in Table 3). Thus, all state variable

677 estimations below proceed with the prior knowledge of an upper and lower bound. There are several

678 convergence criteria that can be used with the L-BFGS-B, including an absolute threshold on the

679 cost function and a relative (per iteration) threshold. In all experiments, these are set to low values,

680 which means that more iterations might be employed than strictly necessary in any operational

681 context, but making sure that the global minimum (or very close to it) is reached in each estimation.

682 Because of the additional costs of processing full bandpass functions, all 'initial' processing is

683 performed using the median (1 nm) wavelength of each waveband. A 'polishing' step is then

684 performed to achieve convergence from this starting value, using the full bandpass sampling. The

685 effect of applying the full bandpass functions tends to be generally quite minor.

686

687 We have initially tested the system without observational noise and confirm that the scheme

688 retrieves the truth to within the bounds implied by the convergence criteria and machine precision.

689 Processing time for a single set of 73 time samples with MSI spectral sampling, solving for 6 state

690 vector elements for each day of the year (2190 in total), is currently several hours on a 3 GHz Intel

691   processor on a single core, but this is partially due to very stringent convergence criteria used whilst

692   testing the code and partially because this prototype implementation requires some significant

693   efforts in computer code optimisation.

694

695   In all experiments, we set the prior estimate of the state vector to the values shown in table 2, with

696   very large diagonal uncertainty terms (8). This effectively removes the prior constraint from

697   consideration in these experiments, as we wish to conduct experiments based only on model and

698   observational constraints here.

699

700   In the following sections, we examine the result of applying the weak constraint variational data

701   assimilation approach described above to the synthetic dataset. For all cases, we assume that the

702   uncertainty in the observations is known and that it is Gaussian and uncorrelated between

703   wavebands and between dates. In the first case (3.2), we solve for state vector estimates assuming

704   no dynamic model constraint other than the weak prior (standard deviation 8). This acts as a

705   baseline for further experiments. In the second case (3.3) we assume that model uncertainty g is

706   unknown and attempt to solve for it and the state vector for each day in the year with a form of

707   cross-validation exercise using the SPOT-5 HRV synthetic observations. The 'true' values of g for

708   individual state vector elements are shown in Table 5. The DA is performed with the 'complete' (i.e.

709   5-day sampling MSI) dataset in that case. Finally, we repeat that experiment for the 'cloudy' dataset

710   (3.4).

711

712   TABLE 5 ABOUT HERE

713

714   Graphical results (figures 1-2) are presented as untransformed biophysical variables (i.e. LAI, C_{ab},

715   C_w, C_{dm} , N and s_1), showing: the 'true' ('original') state vector (dashed line); circles and error bars

716   (shaded region) shows mean and 95% credible interval bounds (at plus/minus 1.96 standard

717   deviations). We will term 1.96 standard deviations 'uncertainty' for the remainder of the paper,

718   unless the statement is otherwise qualified. The uncertainty bounds are slightly larger for the upper

719   limits than for the lower limits (other than for N and s_1) due to the nature of the transformations

720   used in the approximate linearization (table 3). Tabular results for the experiments (tables 9-12) are

721   expressed in transformed parameter space, as that is the space in which the state vector is inferred

722   and in which the Gaussian statistics derived are most natural.

723

724   **3.2 Baseline estimates**

725   We first produce a baseline estimate of the six state variables over the 73 time periods in the year,

726   assuming no constraint to the solution other than the bounds noted above, the (noisy) observations,

727   knowledge of the uncertainty in the observations, and the weak prior constraint.

728

729   The results for the baseline experiment are produced using the EO-LDAS system with each

730   observation set (i.e. all wavebands, but only one angular sample) independently. The algorithm

731   requires an initial guess of the state vector and iterates to its final estimate. The initial estimate of

732   the state vector in each case and all subsequent estimates is taken as the value used in the prior

733   constraint.

734

735   FIGURE 1 ABOUT HERE

736

737   In figure 1, the column titled 'single obs inversion' shows the results of this state vector estimate for

738   the six parameters that are varied, transformed back to their biophysical meanings (through the

739   inverse of the functions in table 3). The sub-plots rows show results for the observation operator

740   parameters LAI, C_{ab}, C_w C_{dm}, N and s_1 respectively. The uncertainty (average credible interval)

741   associated with each (transformed) parameter for the baseline experiment is given in table 6 ('single

742   obs.'). Relating these uncertainties to the parameter ranges (table 4), we note that they are around

743 5% for TLAI, 10% for s_1 and TC_{ab} respectively for dates where there are observations, more than

744 20% for (transformed) leaf water and dry matter content and around 33% for N. We can suppose

745 these then to be typical uncertainty values for MSI sampling (with the assumed noise

746 characteristics). The cross correlation associated with these, illustrated in table 7 are highly variable

747 from one sample to the next. The median values given show quite strong negative correlations

748 between TLAI and TC_{ab} and TC_w but positive correlations with s_1 and TC_{dm}. The median s_1 shows

749 negative correlations with all terms other than TLAI. Despite the fact that the average transformed

750 LAI uncertainty is only around 5%, we can see if figure 1 that both the error and uncertainty can be

751 rather high. Around peak LAI, results from individual samples vary by around LAI 2.5 and there is

752 a general tendency to underestimate. The general trends of C_{ab} and C_w are discernable, but there is

753 large variation and large uncertainty. The terms that are supposed to be constant here, C_{dm} and N

754 depart significantly from their true state and the negative correlation is evident in the state

755 trajectories around the central part of the year.

756

757 TABLE 6 ABOUT HERE

758 TABLE 7 ABOUT HERE

759

760 How then can we improve on this situation? The ways to reduce uncertainty are to have data with

761 lower noise characteristics, to average or smooth in some way, or to add other constraints to the

762 solution. In any realistic scenario, we have only limited control of the first of these. Averaging and

763 smoothing then are the general pragmatic responses to such issues. If however this is performed *ad*

764 *hoc* as a post processing step to any individual term (e.g. only LAI) this would not take account of

765 the cross correlation in the uncertainties which can only give sub-optimal results.

766

767 In spite of these quite high levels of uncertainty (and correlation of uncertainty) for these estimates,

768 there is clearly quite a strong correlation between the values of the state vector and its neighbours in

time. The general underlying patterns are apparent in the 'complete' scenario, although much of the (potentially important) detail will be lost in a more realistic 'cloudy' scenario. The enhancement of this temporal correlation effect and the suppression of the noise are at the heart of all regularisation approaches and the essence of weak constraint data assimilation. If we have some model ('expectation') of the temporal trajectory of the state vector, then we can use this to filter the unwanted noise. As noted above, this may be a model based on our understanding of radiation interception and biogeochemical cycling (e.g. Quaife et al., 2008) driven by some set of external (environmental) parameters, or it may simply be some parametric curve that we believe can mimic e.g. the phenological development of LAI. In either case, what DA aims to achieve is an optimal merging of such models (through the adjustment of the state vector or essentially a calibration of the parameters controlling the development of state in the model) and the observations. For land surface monitoring, there are several options for such models for LAI development as mentioned, and up to a point for some other state variables (e.g. soil moisture), but there is very little to guide information extraction on many other state variables that affect the observations (e.g. leaf chlorophyll concentration or dry matter). In such a case, we need to develop simple methods, within a DA framework. Fortunately, there are many to choose from, although as Twomey (2002) points out, the results are likely to be similar for most of these methods: indeed, it would be worrying if they were not.

3.3 DA: Complete scenario

Here, we apply first order and second order derivative constraints to the solution, but we expect the results to be broadly similar. In both cases, we need only supply some estimate of the uncertainty associated with these constraints through the smoothness term g to achieve a regularised solution to the state vector estimate. These constraints are applied by incorporating a model that, in the absence of any observations, would set the first (second) derivatives of the state variables to zero. Assuming that we apply the same (strength of) constraint to the whole time series, we need to supply an

795   estimate of the mean squared first (second) difference in the parameter values (true values in table

796   5). For the first (second) difference then, this can be thought of as an estimate of the uncertainty in a

797   zero-order (first-order) process model over one time step as noted above.

798

799   We use a form of cross-validation to estimate g. This is achieved with a synthetic dataset from an

800   alternative SPOT-5 HRG-like sensor. The core of the exercise then is a comparison between these

801   synthetic data (driven by the 'true' values of the state vector, plus random noise as above) and a

802   simulation of the same sensor wavebands and acquisition geometry driven by the state vector

803   estimated from the synthetic data from Sentinel-2 MSI. We choose this cross validation sensor as

804   one different to MSI to stress that one role of a DA system of this sort can be to provide simulated

805   data of sensors other than those used in the DA exercise. Here, we measure the average squared

806   difference between the synthetic HRG data and the DA simulated observations, weighted by the

807   uncertainty in the synthetic data, and term this RMSE in cross-validation. The locations of the

808   synthetic HRG observations are indicated in the lower panel of figure 1 by + symbols.

809

810   FIGURE 2 ABOUT HERE

811

812   Figure 2 shows the error in cross-validation as a function of g for the model first- and second-order

813   difference constraints for the complete case (black circles and squares respectively). There are clear

814   minima for these functions, which provide estimates of the optimal model uncertainty (averaged

815   over all terms). Also shown in the figure is a set of vertical lines that represent the theoretical value

816   of the smoothness term for each of the state vector elements that vary over time (from table 5). For

817   the first order constraint, the minimum of the cross validation function is g=150 which is very close

818   to the theoretical values. For the second order constraint the cross validation RMSE minimum at

819   g=530 is rather less than the theoretical values. For both cases however, we observe a very broad

820   minimum, so there is quite a large range of values of g that allow almost equally good prediction of

821   the synthetic cross validation HRG observations.

822

823   TABLE 8 ABOUT HERE

824

825   Tables 8 provides statistics on the uncertainty reduction, (the posterior uncertainty estimate from the

826   DA relative to that after solving for each sample separately and assuming the prior uncertainty

827   where there are no observations). The average improvement in uncertainty is 4.07 for the first order

828   constraint and 2.73 for the second order difference constraint. This is very significant but it must be

829   remembered that 4/5 of the samples in the 'single obs' solution have only the prior constraint and

830   uncertainty. Examining only locations where observation lie (i.e. ignoring interpolation

831   performance relative to the *a priori* estimate), we see the uncertainty reduction drop by nearly 50%

832   in this case, down to 2.20 for the first order constraint and 1.30 for the second difference constraint.

833   From those figures, we would suppose the first order constraint to be greatly superior to the second

834   order constraint, but if we look at the plots in figure 1, the second order constraint results seem to

835   have more reasonable uncertainty bounds than the other results. This is at least partially because the

836   apparent uncertainty resulting from the DA is strongly dependent on the value of g used in the

837   model constraint: the higher the value of g, the smoother will be the solution and the lower the

838   estimate of uncertainty. The only check we have done on the *veracity* of the solution comes from

839   the cross validation, which is an indirect check: in any non-synthetic experiment we rarely know the

840   'truth' to any great degree of certainty. Since we have a synthetic experiment here, we can however

841   test how frequently the derived solution matches the (synthetic) truth within the claimed uncertainty

842   bounds. One reasonable summary measure of this is the percentage of true values of state vector

843   elements that lie within the 95% credible interval claimed by the DA results. These are shown in

844   table 8. We can see that for the 'single obs' estimates (no regularisation), only around 64% of the

845   state vector lies within the 95% credible interval claimed by the solution. The figure is as low as

846   58% for TC_{dm}. We can suppose the   average estimated uncertainty then to be only around 67% of

847   the true value, i.e. we should inflate the estimated uncertainty by a factor of around 1.5. This would

848   apply equally to the results in table 6. We see almost the same value for the first order constraint,

849   which suggests the reduction in uncertainty by a factor of 2.2 is likely true. For the second order

850   difference constraint however, around 84% (table 8) of the sample lie within the uncertainty bounds,

851   so here, a better estimate of the uncertainty reduction might be around 1.70 rather than the 1.30

852   reported. This apparent under-reporting of the uncertainty is worthy of comment and there could be

853   several reasons for this. One explanation could be that we are simply under-estimating the

854   uncertainty from the approximations made when calculating the Hessian for the observation

855   operator. A more likely reason is non-linear effects in the treatment of uncertainties. In spite of our

856   attempt to account for gross non-linear impacts through parameter transformations, residual non-

857   linear effects may be causing this under-estimation of uncertainty by a factor of around 1.5.

858

859   FIGURE 3 ABOUT HERE

860   FIGURE 4 ABOUT HERE

861

862   **3.4 DA: Cloudy scenario**

863   Figure 3 shows the DA results for the cloudy scenario. This is a much more realistic test for a DA

864   system. The task now is not only to reduce the uncertainty at the points where we have observations

865   but also to try to provide an effective interpolation over data gaps. The cross validation plots for this

866   case are shown in figure 2 (white circle and square) and provide a much more narrow minimum.

867   This implies that to achieve acceptable results in cross validation, the range of g values that can be

868   tolerated is much more restricted. The minima of these functions however are well within the

869   bounds of the cross validation results for the 'complete' scenario and the optimal g indicated very

870   similar to that obtained from the previous results. This indicates that the method for estimating g is

871   quite robust, even when there are large data gaps. Unsurprisingly, the absolute value of the cross

872   validation RMSE is higher for the cloudy case, indicating poorer performance in prediction for this

873   lower quality dataset.

874

875   TABLE 9 ABOUT HERE

876

877   Table 9 shows the reduction in uncertainty for this experiment. One striking feature of these is that

878   the percentage of cases within the credible interval is now above 80% in both cases, meaning that

879   the reported uncertainties are close to the true values. Whilst the apparent reduction in uncertainty is

880   apparently quite small (indeed, there is an increase in uncertainty for some state vector elements) at

881   1.53 for the first order constraint and 1.14 for the second order, when weighed against the improved

882   statistical representation, these rise to values directly comparable with the results from the previous

883   experiment. The credible intervals shown in figure 3 are now realistic representations of the state

884   vector elements and their uncertainties, achieved with only 50% of the samples of the previous

885   experiment and with large data gaps, which is an important result.

886

887   Figure 4 shows the posterior correlation matrices (the inverse Hessian matrix) for the cloudy

888   scenario. The general pattern of this matrix for the 'complete' scenario is rather similar so not

889   shown here. Obviously, the correlation is unity along the leading diagonal. Another important

890   feature is that the broad patterns of positive and negative correlations that we noted for the 'single

891   obs' solutions remains here. There is negative correlation between s_1 and all terms by TLAI. There

892   is negative correlation between TLAI and TC_{ab} and TC_w but positive correlation with TC_{dm}. These

893   patterns are consistent for both constraints used. We notice then that the application of the dynamic

894   model (regularisation) in time does not remove the correlations arising from the inverse Hessian of

895   the observation cost function, but rather it 'spreads' uncertainty correlation out in the time domain.

896   This is particularly visible in the second order constraint matrix in figure 4 where we can clearly see

897   this smoothing being greater where there are data gaps (s_1 is a good example of that). Equally,

898   where a part of the state vector has been strongly influenced by the regularisation (e.g. N for the

899 first order constraint) we see very high correlation at all time steps. Another interesting feature of

900 this figure is the fact that for some state vector elements (e.g. N for the second order constraint) we

901 can clearly see the influence of the periodic boundary condition).

902

903 **4 Discussion**

904 **4.1 The value of an EO-LDAS**

905 This paper outlines a scheme for a weak constraint data assimilation system, developed in the ESA

906 EO-LDAS project, designed for integrating Earth Observation data from a variety of sources over

907 arbitrary time scales, and through that to multiple spatial resolutions. It has the potential, via careful

908 definition of the underlying model to be extended to spatial constraints, although this is not

909 explored here. The scheme is designed to allow interface with process models, should they be

910 available, though only an empirical regularisation model is shown in this paper. The core of the

911 system is a set of constraints on: (i) prior estimates of the state vector; (ii) a linear model of the state

912 vector; (iii) observation operator (RT model) predictions of a set of EO data and a DA scheme

913 around these using an iterative bounded optimisation approach (L-BFGS-B).

914

915 In this paper, we have set up and run a synthetic data experiment with EO data mimicking those that

916 might be provided by the MSI sensors on the forthcoming Sentinel-2 platforms. Experiments in DA

917 are conducted for an idealised 'full coverage' scenario (5 day sampling) and for a 'cloudy' case

918 (average around 10 day sampling but with large data gaps of up to 60 days). The results are

919 compared to baseline experiments where we attempt to estimate the state variable trajectories over

920 the course of a year for a subset of the total state variables (six elements per observation period).

921 The prior term is used only very weakly here, although bounds are set to the state vector elements.

922 Further, we assume that we have direct access to the surface reflectance (as opposed to top of

923 atmosphere radiance), and that the noise on the observations is uncorrelated and of known

924 magnitude. Broadly however, we can claim that the baseline results should be indicative of those

925   that might be obtained from Sentinel-2 data using 'traditional' estimation methods. For what we

926   suppose to be a typical observation noise scenario, the uncertainty can be a quite large proportion of

927   the signal for important terms such as LAI, this for a peak LAI of only around 3.7, although on

928   average the uncertainty in TLAI may only be around 5%. This then, relates to the information

929   content of a single MSI observation for this level of noise, assuming some important terms such as

930   leaf angle distribution are known precisely. These results are not surprising but are simply a

931   manifestation of the difficulty of the inference of biophysical parameters from remote radiometric

932   observations: the problem may often be ill-posed (consider the situation if only two wavebands at

933   red and near infrared were available), but even if it is not strictly so, there may not be sufficient

934   information to very well constrain the information we require. In any case, there can be quite high

935   correlation in uncertainty.

936

937   The ways to improve this situation are: (i) to obtain more observations (although more observations

938   does not always translate to more information: consider again sampling at only red and near

939   infrared wavelengths in trying to constrain e.g. leaf water content); or (ii) to add some other forms

940   of information; (iii) average the data. Much *a priori* information has been used in the past to help

941   constrain these problems, but this has often been approached in a rather *ad hoc* manner. Examples

942   include: assuming some terms known, without considering the impact of uncertainty in these, or

943   imposing degrees of smoothness; assuming that some terms are constant over some arbitrary time

944   period; or *post hoc* low pass filtering to the final results. Given its success in other field of science

945   and engineering, many authors have proposed that DA should be seen as the route to integration of

946   the various forms of information one might wish to use to constrain the estimation. Key to DA is the

947   weighting between the various sources of evidence, and key to this is assigning uncertainty

948   correctly to the sources. This is a feature of the approach that dramatically differentiates it from the

949   way in which VIs are mostly used in EO. As we note in the introduction, if we wish to estimate

950   biophysical parameters (such as LAI) there is generally some form of calibration (against ground

951 observations or RT model runs) but it is extremely rare that those model uncertainties are

952 considered in mapping the product. Other processing steps such as angular normalisation may have

953 taken place, but again, any concepts of uncertainty arising from these are on the whole disregarded.

954 All of these issues *could* be addressed within a DA framework, even if the source of the EO

955 information were to be VIs.

956

957 If a biophysical process model is available to predict the development of the state variables that

958 control the remote sensing signal, this can clearly add information to help constrain the problem. If

959 information from the observations feed back to improve the estimates of the parameters controlling

960 the process model or alternatively improve the state estimates, then a better integration of

961 observations and model is achieved, which will likely better constrain additional terms estimated by

962 the process model. This has been argued by Quaife et al. (2008) and others who have worked on

963 integrating EO data and e.g. Carbon flux process models. However, models such as these simply do

964 not provide information on a large number of the variables that affect EO signals, and this is likely

965 to remain the case for the foreseeable future. Exercises in EO-model integration then

966 understandably tend to focus of the points of common linkage (which often is no more than LAI,

967 being supposed linearly related to leaf Carbon) and then applying the 'traditional' methods to the

968 remaining parameters (assuming them known or at best constant over time). In this paper, and in the

969 EO-LDAS work in general, we have taken the focus away from working with some specific process

970 model, and tried to consider the more general case and the sorts of constraints that might be

971 appropriate. If no physical model is available, empirical concepts of smoothness in the state

972 variables come to the fore. These ideas become even more important if one considers constraint in

973 the spatial domain, where physical or even biological process models are almost completely lacking

974 to aid biophysical parameter estimation.

975

976 The EO-LDAS scheme that we have built is capable of using any linearised process model and of

more general interface to process model codes provided the cost function and its derivatives can be calculated. In the prototype and in this paper we have examined first- and second-order derivative constraints as general, appropriate (empirical) models for biophysical parameter estimation in DA. We have simulated typical profiles of LAI and leaf chlorophyll concentration and rather complex profiles of leaf water concentration and soil brightness and shown that with Sentinel-2 MSI data every 5 days, a reduction in uncertainty by a factor of around 2 might generally be achieved. More interestingly perhaps, after compensation for errors in uncertainty prediction, we saw that similar reductions might be achieved even when there are large data gaps and 50% of the samples lost due to cloud cover.

We have also demonstrated (figure 2) that it is feasible to estimate the required hyper-parameters from some form of cross-validation exercise to impose an appropriate degree of model uncertainty, and that quite consistent results can be obtained even under cloudy conditions. This is an important practical point for the eventual operationalisation of these methods, but the area requires a little more discussion of practical issues in its implementation.

Approximate linearization of the RT model variables here, following Weiss et al. (2000), has allowed Gaussian distributions to be assumed throughout. Although we have not directly investigated any residual non-linear effects in this study, some evidence is provided that on average we may be predicting only around 2/3 of the true uncertainty.

4.1 Future directions

In this paper, we have only demonstrated DA for a homogeneous observation system, i.e. one for which we have assumed the spectral sampling (and in effect, spatial resolution) for all observations is the same. Using the EO-LDAS prototype for spectrally heterogeneous systems is straightforward, but further work is needed to test the multi-scale concepts that would more generally be required.

1003 Within the existing prototype, the state vector can represent any mixture of temporal or spatial

1004 samples. The concepts of temporal smoothness used here apply equally to the spatial domain

1005 (indeed, such ideas form the basis of the field of geostatistics (e.g. Atkinson and Lewis, 2000)), so

1006 the prototype can be used directly to link a state vector representation on a spatial grid, via

1007 appropriate specification of the matrix A. Indeed, one could consider the experiments performed in

1008 this paper simply as being on a spatial transect, rather than as we have assumed a temporal sampling

1009 pattern. The only practical difference is that in that case, the viewing and illumination angles would

1010 be near identical for all samples.

1011

1012 The EO-LDAS prototype is designed to allow a (relatively) large number of state variables to be

1013 estimated simultaneously in a variational system (> 2000 demonstrated here). One potential

1014 advantage of this is that information can be passed between any of the state vector elements. In

1015 practice, we have only used rather local information transfer in the model constraints applied here

1016 (differences with neighbours in time) and this approach could also be implemented as a sequential

1017 smoother. In viewing the temporal experiment we have performed as effectively equivalent to a

1018 spatial experiment, the neighbourhood need not be very different (i.e., in the spatial sense, we could

1019 follow the approach here and directly connect information in one grid cell to its 8 neighbours).

1020 However, this variational system maintains the capacity for more distant (time or space)

1021 connections, for example in applying multiple scale constraint.

1022

1023 A point that we have not dwelt on in this paper is the time required for processing. This is currently

1024 around several hours for solving for > 2000 state vector elements using 73 samples for what equates

1025 to a single pixel (albeit for all samples over a year). The experiments in this paper were conducted

1026 over around 120 UNIX cores, so quite large-scale experiments are feasible using University

1027 computing resources. Clearly the processing requirements would need to be greatly reduced if such

1028 a system were to be proposed for operational processing. The computer code is not on the whole

1029 written to be fast, but rather to be adequate to learn about using this form of DA. There are various

1030 ways in which this might be tackled: clearly the very tight convergence criteria could be somewhat

1031 relaxed, and more efficient codes could be written, but there will always be a relatively large

1032 overhead on multiple calculations of a radiative transfer model. Pragmatic ways to overcome this

1033 issue have mainly in the past dealt with using LUTs or ANNs to sample or approximate the

1034 observation operator, but clearly in the DA framework we must consider representational error in

1035 any such emulation. One avenue that holds much promise is that of Gaussian Process (GP)

1036 emulators (Kennedy and O'Hagan, 2000, 2001), a form of regression that has been successfully

1037 used to simulate computationally costly models runs through simple functional approximations. The

1038 great benefit of this latter approach is that uncertainties in the emulated model are included and that

1039 derivatives of the model can also be easily produced. If we consider the observation operator as a

1040 sampled function with GP emulation, it is interesting to note that the underlying concepts implying

1041 smooth interpolation with treatment of representation uncertainty are of course the same as we are

1042 performing in the temporal (or indeed spatial) process model in the DA.

1043

1044 **5 Conclusions**

1045 The EO-LDAS prototype that is described in this paper has been demonstrated to be capable of

1046 simultaneously estimating a state vector of over 2000 elements of surface biophysical

1047 characteristics in a synthetic experiment using simulated Sentinel-2 MSI data. Although the

1048 processing time required for this is currently a little long, this is a significant step in the size of such

1049 problems that can be tackled simultaneously. The ability to do this derives from the use of AD-

1050 generated adjoint code for the observation operator at the heart of the DA system.

1051

1052 The DA scheme that has been developed is a weak constraint variational system. The value of such

1053 a scheme has been demonstrated using the synthetic MSI data to show a reduction in uncertainty of

1054 up to around 2 when a linear dynamic model is used in the DA. The linear dynamic model is

proposed as a general implementation that can potentially be interfaced to biophysical process models through linearization. It is used in this paper with first and second-order derivative constraints (zero- and first-order process models) which are shown to be sufficient to track rather complex biophysical parameter trajectories via a radiative transfer model 'observation operator' interface to the synthetic EO data.

We have noted at various points in this text, that some aspects of the EO-LDAS prototype are still under development of testing, but what actually is provided by the prototype code is a functioning tool for exploring many issues in DA and for estimating information on surface biophysical parameters. The tool is designed as a weak constraint variational system, but we have argued that it can also be used sequentially as it stands. We have demonstrated the use of the tool and of DA concepts in reducing uncertainty in biophysical parameter estimation in a temporal sense, but also argued the equivalence of this (in DA in general, but in the tool specifically) for the spatial domain as well. We have used only empirical 'regularisation' concepts in demonstrating the DA, but noted that these are powerful general concepts that are extremely useful, particularly if biophysical models do not treat some of the parameters we are concerned with. In the more general case though, any linearization of a more process-driven model can be directly interfaced to the EO-LDAS prototype.

There is clearly quite a long way to go from initial experiments with relatively slow computer codes to an operational system for land data information extraction from EO, i.e. an operational EO-LDAS, but the concepts explored here demonstrate the power and potential flexibility of such an approach.

Acknowledgements

References

Asrar, G., Kanemasu, E.T., Jackson, R.D., Pinter Jr, P.J., 1985. Estimation of total above-ground phytomass production using remotely sensed data. Remote Sensing of Environment 17, 211–220.

Atkinson, P. and Lewis, P., 2000, Geostatistical classification for remote sensing: an introduction. Computers and Geoscience, 26(4), 361-371.

Baret, F. and Guyot, G., 1991. Potentials and limits of vegetation indices for LAI and APAR assessment. Remote Sensing of Environment 35, 161–173.

Behrenfeld, M.J., Randerson, J.T., McClain, C.R., Feldman, G.C., Los, S.O., Tucker, C.J., Falkowski, P.G., Field, C.B., Frouin, R., Esaias, W.E., others, 2001. Biospheric primary production during an ENSO transition. Science 291, 2594.

Beven, K., 2006. A manifesto for the equifinality thesis. Journal of Hydrology 320, 18–36.

Byrd, R.H., Lu, P., Nocedal, J., Zhu, C., 1995. A limited memory algorithm for bound constrained optimization. SIAM Journal on Scientific Computing 16, 1190–1208.

CEOS, 2011a. The CEOS Constellation for Land Surface Imaging [WWW Document]. URL http://wgiss.ceos.org/lsip/lsic.shtml, accessed 18/11/2011.

CEOS, 2011b, CEOS EO Handbook – Instrument summary: HRG. [WWW Document]. URL http://database.eohandbook.com/database/instrumentsummary.aspx?instrumentID=183 accessed 18/11/2011.

Chen, J.M., Pavlic, G., Brown, L., Cihlar, J., Leblanc, S.G., White, H.P., Hall, R.J., Peddle, D.R., King, D.J., Trofymow, J.A., others, 2002. Derivation and validation of Canada-wide coarse-

resolution leaf area index maps using high-resolution satellite imagery and ground measurements. Remote Sensing of Environment 80, 165–184.

Choudhury, B.J., 1987. Relationships between vegetation indices, radiation absorption, and net photosynthesis evaluated by a sensitivity analysis. Remote Sensing of Environment 22, 209–233.

Clerici, M., Vossbeck, M., Pinty, B., Kaminski, T., Taberner, M., Lavergne, T., Andredakis, I., 2010. Consolidating the two-stream inversion package (JRC-TIP) to retrieve land surface parameters from albedo products. Selected Topics in Applied Earth Observations and Remote Sensing, IEEE Journal of 3, 286–295.

Combal, B., Baret, F., Weiss, M., Trubuil, A., Mace, D., Pragnere, A., Myneni, R., Knyazikhin, Y., Wang, L., 2003. Retrieval of canopy biophysical variables from bidirectional reflectance:: Using prior information to solve the ill-posed inverse problem. Remote Sensing of Environment 84, 1–15.

Council of the European Union, 2010. Taking forward the European Space Policy.

DMCII, 2010. DMC Constellation [WWW Document]. URL http://www.dmcii.com/about_us_constellation.htm, accessed 20/12/2010.

Eilers, P.H.C., 2003. *A perfect smoother*, Analytical Chemistry, 75(14), pp. 3631-3636

Enting, I.G., 2002. Inverse problems in atmospheric constituent transport. Cambridge University Press.

ESA, 2010. Mission Requirements Document GMES Sentinel-2 [WWW Document]. URL http://esamultimedia.esa.int/docs/GMES/Sentinel-2_MRD.pdf, accessed 20/12/2010.

European Comission, n.d. GEOSS: Policy relevance, Future Challenges, EU contribution to GEOSS, Relevant documentation [WWW Document]. GEOSS. URL http://ec.europa.eu/research/environment/index_en.cfm?section=geo&pg=geoss, accessed 20/12/2010.

Evensen, G., 2003. The ensemble Kalman filter: Theoretical formulation and practical implementation. Ocean dynamics 53, 343–367.

Fang, H., Liang, S., Hoogenboom, G., Teasdale, J., Cavigelli, M., 2008a. Corn-yield estimation

through assimilation of remotely sensed data into the CSM-CERES-Maize model. International Journal of Remote Sensing 29, 3011.

Fang, H., Liang, S., Townshend, J.R., Dickinson, R.E., 2008b. Spatially and temporally continuous LAI data sets based on an integrated filtering method: Examples from North America. Remote Sensing of Environment 112, 75-93.

Féret, J.B., François, C., Asner, G.P., Gitelson, A.A., Martin, R.E., Bidel, L.P., Ustin, S.L., le Maire, G., Jacquemoud, S., 2008. PROSPECT-4 and 5: Advances in the leaf optical properties model separating photosynthetic pigments. Remote Sensing of Environment 112, 3030–3043.

Fung, A.K. and Chen, K., 2010. Microwave Scattering and Emission Models for Users, 1st ed. Artech House Publishers.

Garrigues, S., Lacaze, R., Baret, F., Morisette, J.T., Weiss, M., Nickeson, J.E., Fernandes, R., Plummer, S., Shabanov, N.V., Myneni, R.B., others, 2008. Validation and intercomparison of global Leaf Area Index products derived from remote sensing data. Journal of Geophysical Research, 113, G02028.

Ghil, M. and Malanotte-Rizzoli, P., 1991. Data assimilation in meteorology and oceanography. Adv. Geophys 33, 141–266.

Giering, R. and Kaminski, T., 1998. Recipes for adjoint code construction. ACM Transactions on Mathematical Software (TOMS) 24, 437–474.

Gill, P.E., Murray, W., Wright, M.H., 1981. Practical optimization. Academic Press, London and New York.

Gobron, N., Pinty, B., Verstraete, M.M., Govaerts, Y., 1997. A semidiscrete model for the scattering of light by vegetation. Journal of Geophysical Research 102, 9431–9446.

Gobron, N., Pinty, B., Verstraete, M., Widlowski, J., 2000. Advanced vegetation indices optimized for up-coming sensors: Design, performance, and applications. IEEE Transactions on Geoscience and Remote Sensing, 38, 2489-2505.

Gobron, N., Pinty, B., Verstraete, M.M., Widlowski, J.L., 2002. Advanced vegetation indices

optimized for up-coming sensors: Design, performance, and applications. IEEE Transactions on Geoscience and Remote Sensing, 38, 2489–2505.

Gobron, N., Belward, A., Pinty, B., Knorr, W., 2010. Monitoring biosphere vegetation 1998–2009. Geophysical Research Letters 37, L15402.

Goel, N.S., 1988. Models of vegetation canopy reflectance and their use in estimation of biophysical parameters from reflectance data. Remote Sensing Reviews 4, 1–212.

Goel, N.S., Thompson, R.L., 2000. A snapshot of canopy reflectance models and a universal model for the radiation regime. Remote Sensing Reviews 18, 197–225.

Goward, S.N., Tucker, C.J., Dye, D.G., 1985. North American vegetation patterns observed with the NOAA-7 advanced very high resolution radiometer. Plant Ecology 64, 3–14.

Jacquemoud, S., Baret, F., 1990. PROSPECT: A model of leaf optical properties spectra. Remote Sensing of Environment 34, 75–91.

Kennedy, M.C., O'Hagan, A., 2001. Bayesian calibration of computer models. Journal of the Royal Statistical Society: Series B (Statistical Methodology) 63, 425–464.

Kennedy, M.C., O'Hagan, A., 2000. Predicting the output from a complex computer code when fast approximations are available. Biometrika 87, 1.

Kimes, D.S., Knyazikhin, Y., Privette, J.L., Abuelgasim, A.A., Gao, F., 2000. Inversion methods for physically-based models. Remote Sensing Reviews 18, 381–439.

Knorr, W., Kaminski, T., Scholze, M., Gobron, N., Pinty, B., Giering, R., Mathieu, P., 2010. Carbon cycle data assimilation with a generic phenology model. Journal of Geophysical. Research, 115, G04017.

Kuusk, A., 1995. A fast, invertible canopy reflectance model. Remote Sensing of Environment 51, 342–350.

Lavergne, T., Kaminski, T., Pinty, B., Taberner, M., Gobron, N., Verstraete, M.M., Vossbeck, M., Widlowski, J.L., Giering, R., 2007. Application to MISR land products of an RPV model inversion package using adjoint and Hessian codes. Remote Sensing of Environment 107, 362–375.

1185 Lewis, P. and Disney, M., 2007. Spectral invariants and scattering across multiple scales from

1186 within-leaf to canopy. Remote Sensing of Environment 109, 196–206.

1187 Liang, S. and Strahler, A.H., 2002. An analytic BRDF model of canopy radiative transfer and its

1188 inversion. IEEE Transactions on Geoscience and Remote Sensing, 31, 1081–1092.

1189 Lu, X., Liu, R., Liu, J., Liang, S., 2007. Removal of noise by wavelet method to generate high

1190 quality temporal data of terrestrial MODIS products. Photogrammetric Engineering and Remote

1191 Sensing 73, 1129.

1192 Lubansky, A. S., Yeow, Y. L., Leong Y-K., Wickramasinghe S. R., Han B., 2006. A general method

1193 of computing the derivative of experimental data., AIChe J., 52, pp. 323-332.

1194 Lyapustin, A. and Knyazikhin, Y., 2001, Method of Green Function in the Radiative Transfer

1195 Problem. Part I: Homogeneous non-Lambertian Surface. Applied Optics, 40, 3495-3501.

1196 Lyapustin, A., Wang, Y., Martonchik, J., Privette, J., Holben, B., Slutsker, I., Sinyuk, A. and

1197 Smirnov, A., 2006, Local analysis of MISR surface BRF and albedo over GSFC and Mongu

1198 AERONET sites, IEEE Transactions on Geoscience and Remote Sensing, 44, 1707-1718.

1199 McLaughlin, D., 2002. An integrated approach to hydrologic data assimilation: interpolation,

1200 smoothing, and filtering. Advances in Water Resources 25, 1275–1286.

1201 Myneni, R.B., Maggion, S., Iaquinta, J., Privette, J.L., Gobron, N., Pinty, B., Kimes, D.S.,

1202 Verstraete, M.M., Williams, D.L., 1995. Optical remote sensing of vegetation: Modeling, caveats,

1203 and algorithms. Remote Sensing of Environment 51, 169-188.

1204 NASA, 2010. NASA - A-Train [WWW Document]. URL

1205 http://www.nasa.gov/mission_pages/cloudsat/multimedia/a-train.html

1206 Nemani, R.R., Keeling, C.D., Hashimoto, H., Jolly, W.M., Piper, S.C., Tucker, C.J., Myneni, R.B.,

1207 Running, S.W., 2003. Climate-driven increases in global terrestrial net primary production from

1208 1982 to 1999. Science 300, 1560.

1209 Olioso, A., Inoue, Y., Ortega-Farias, S., Demarty, J., Wigneron, J.P., Braud, I., Jacob, F.,

1210 Lecharpentier, P., Ottlé, C., Calvet, J.C., others, 2005. Future directions for advanced

evapotranspiration modeling: Assimilation of remote sensing data into crop simulation models and SVAT models. Irrigation and Drainage Systems 19, 377–412.

Pinty, B., Lavergne, T., Vossbeck, M., Kaminski, T., Aussedat, O., Giering, R., Gobron, N., Taberner, M., Verstraete, M.M. and Widlowski, J-L. (2007) Retrieving surface parameters for climate models from Moderate Resolution Imaging Spectroradiometer (MODIS)-Multiangle Imaging Spectroradiometer (MISR) albedo products, Journal of Geophysical. Research, 112, D10116, doi:10.1029/2006JD008105.

Price, J.C., 1990. On the information content of soil reflectance spectra. Remote sensing of Environment 33, 113–121.

Privette, J.L., Myneni, R.B., Tucker, C.J., Emery, W.J., 1994. Invertibility of a 1-D discrete ordinates canopy reflectance model. Remote Sensing of Environment 48, 89–105.

Qin, J., Liang, S., Li, X., Wang, J., 2008. Development of the adjoint model of a canopy radiative transfer model for sensitivity study and inversion of leaf area index. IEEE Transactions on Geoscience and Remote Sensing, 46, 2028–2037.

Qin, J., Liang, S., Liu, R., Zhang, H., Hu, B., 2007. A weak-constraint-based data assimilation scheme for estimating surface turbulent fluxes. IEEE Geoscience and Remote Sensing Letters, 4, 649–653.

Qin, J., Liang, S., Yang, K., Kaihotsu, I., Liu, R., Koike, T., 2009. Simultaneous estimation of both soil moisture and model parameters using particle filtering method through the assimilation of microwave signal. Journal of Geophysical Research 114, D15103.

Quaife, T., Lewis, P., 2010. Temporal Constraints on Linear BRDF Model Parameters. IEEE Transactions on Geoscience and Remote Sensing, 48, 2445–2450.

Quaife, T., Lewis, P., De Kauwe, M., Williams, M., Law, B.E., Disney, M., Bowyer, P., 2008. Assimilating canopy reflectance data into an ecosystem model with an Ensemble Kalman Filter. Remote Sensing of Environment 112, 1347-1364.

Richardson, A.J., Wiegand, C.L., 1977. Distinguishing vegetation from soil background

information(by gray mapping of Landsat MSS data). Photogrammetric Engineering and Remote Sensing 43, 1541–1552.

Rochdi, N., Fernandes, R., 2010. Systematic mapping of Leaf Area Index across Canada using 250-meter MODIS data. Remote Sensing of Environment 114, 1130–1135.

Rodgers, C.D., 2000. Inverse Methods for Atmospheric Sounding : Theory and Practice. World Scientific Publishing Company.

Roy, D.P., Jin, Y., Lewis, P.E., Justice, C.O., 2005. Prototyping a global algorithm for systematic fire-affected area mapping using MODIS time series data. Remote Sensing of Environment 97, 137-162.

Slater, A.G. and Clark, M.P., 2009. Snow data assimilation via an ensemble Kalman filter. Journal of Hydrometeorology, 7, 478-492.

Sobrino, J.A., Jiménez-Muñoz, J.C., Verhoef, W., 2005. Canopy directional emissivity: Comparison between models. Remote Sensing of Environment 99, 304–314.

Stöckli, R., Rutishauser, T., Dragoni, D., O'Keefe, J., Thornton, P.E., Jolly, M., Lu, L., Denning, A.S., 2008. Remote sensing data assimilation for a prognostic phenology model. Journal of Geophysical Research, 113, 19 PP.

Tarantola, A., 2005. Inverse problem theory and methods for model parameter estimation. Society for Industrial and Applied Mathematics.

Tha Paw, U., others, 1992. Development of models for thermal infrared radiation above and within plant canopies. ISPRS Journal of Photogrammetry and Remote Sensing, 47, 189–203.

Tucker, C.J., 1979. Red and photographic infrared linear combinations for monitoring vegetation. Remote sensing of Environment, 8, 127–150.

Twomey, S., 2002. Introduction to the Mathematics of Inversion in Remote Sensing. Courier Dover Publications.

Verhoef, W., Bach, H., 2003. Simulation of hyperspectral and directional radiance images using coupled biophysical and atmospheric radiative transfer models. Remote Sensing of Environment,

1263   87, 23–41.

1264   Vermote, E.F., Tanré, D., Deuzé, J.L., Herman, M., Morcrette, J.J., 1997. Second Simulation of the

1265   Satellite Signal in the Solar Spectrum, 6S: An Overview. IEEE Transactions on Geoscience and

1266   Remote Sensing, 35(3), 675-686.

1267   Vermote, E.F., El Saleous, N.Z., Justice, C.O., 2002. Atmospheric correction of MODIS data in the

1268   visible to middle infrared: first results. Remote Sensing of Environment, 83, 97–111.

1269   Wahba, G., 1990. Spline models for observational data. Philadelphia, Pa: Society for Industrial and

1270   Applied Mathematics.

1271   Weiss, M., Baret, F., Myneni, R.B., Pragnère, A., Knyazikhin, Y., 2000. Investigation of a model

1272   inversion technique to estimate canopy biophysical variables from spectral and directional

1273   reflectance data, Agronomie 20, 3–22.

1274   Widlowski, J.L., Taberner, M., Pinty, B., Bruniquel-Pinel, V., Disney, M., Fernandes, R., Gastellu-

1275   Etchegorry, J.P., Gobron, N., Kuusk, A., Lavergne, T., others, 2007. Third Radiation Transfer Model

1276   Intercomparison (RAMI) exercise: Documenting progress in canopy reflectance models. Journal of

1277   Geophysical Research, 112, D09111.

1278   Xiao, Z., Liang, S., Wang, J., Song, J., Wu, X., 2009. A temporally integrated inversion method for

1279   estimating leaf area index from MODIS data. IEEE Transactions on Geoscience and Remote

1280   Sensing, 47, 2536–2545.

1281   Xiao, Z., Liang, S., Wang, J., Jiang, B., Li, X., 2011. Real-time retrieval of Leaf Area Index from

1282   MODIS time series data. Remote Sensing of Environment 115, 97-106.

1283   Zhu, C., Byrd, R.H., Lu, P., Nocedal, J., 1997. Algorithm 778: L-BFGS-B: Fortran subroutines for

1284   large-scale bound-constrained optimization. ACM Transactions on Mathematical Software (TOMS)

1285   23, 550–560.

1286   Zupanski, D.., 1997, A general weak constraint applicable to operational 4dvar data assimilation

1287   systems, Monthly weather   review, 125, 2274–2292.

1288

1289

1290

Table Captions

Table 1. Spatial resolution, Central wavelength and bandwidths for Sentinel-2 MSI (ESA, 2010).

Table 2. Summary of observation operator state variables.

Table 3. Transformations applied to approximate linearise state variable response.

Table 4. Upper and lower bounds for the state vector terms (in transformed space, where appropriate) used in the simulations, along with the temporal trajectory assumed.

Table 5. Model uncertainty γ for each parameter, calculated from the synthetic model state vector. TC_{dm} and N were kept constant, so have no theoretical model uncertainty associated.

Table 6: Mean posterior uncertainty. Figures refer to the complete daily time series, while figures in brackets refer to the mean posterior uncertainty only considering the dates where observations are available.

Table 7: Single observation posterior correlation matrix. Elements above the main diagonal show the results for DoY 186, whereas the elements below the main diagonal represent the median of all dates.

Table 8: Uncertainty reduction relative to the single observation inversion, as well as percentage of cases where the true parameter lies within the estimated 95% credible interval. Results for non-cloudy scenario are reported. both complete time series.

Table 9: Uncertainty reduction relative to the single observation, as well as percentage of cases where the true parameter lies within the estimated 95% confidence interval. Results for cloudy scenario.

.

Figure Captions

1319 Figure 1. Base level state vector estimated from inverting single observations, (left column) and for

1320 model uncertainty unknown and estimated through cross-validation – first difference constraint

1321 (central column) and second difference constraint (third column). Results for each of the six

1322 parameters are shown in rows. True values are shown as a dashed line. The full lines are the

1323 posterior means, and the shaded area represents the associated +/-1.96 standard deviations interval.

1324 MSI observations are shown as open symbols. Crosses along the bottom of the third row indicate

1325 the location of the cross validation acquisition dates.

1326 Figure 2. Error in cross validation scaled by observational uncertainty for varying model uncertainty

1327 γ for first and second order constraints. Vertical lines around 200 represent the theoretical value of γ

1328 for each of the 4 time-varying state variables using a first order constraint, and vertical lines around

1329 5000 represent the theoretical values for γ for each of the 4 time-varying state variables using

1330 second order constraint.

1331 Figure 3. Base level state vector estimated from inverting single observations, (left column) and for

1332 model uncertainty unknown and estimated through cross-validation – first difference constraint

1333 (central column) and second difference constraint (third column). Reduced number of acquisitions

1334 due to cloud cover scenario. Results for each of the six parameters are shown in rows. True values

1335 are shown as a dashed line. The full lines are the posterior means, and the shaded area represents the

1336 associated +/-1.96 standard deviations interval. MSI observations are shown as open symbols.

1337 Crosses along the bottom of the third row indicate the location of the cross validation acquisition

1338 dates.

1339 Figure 4. Posterior correlation matrices for the cloudy scenario. Labels indicate the location of the

1340 first day for component of the state vector.

1341

1342

Table 1. Spatial resolution, Central wavelength and bandwidths for Sentinel-2 MSI (ESA, 2010).

#	1	2	3	4	5	6	7	8	8a	9	10	11	12
Spatial Resolution / m	60	10	10	10	20	20	20	10	20	60	60	20	20
Wavelength / nm	443	490	560	665	705	740	783	842	865	945	1375	1610	2190
Bandwidth / nm	20	65	35	30	15	15	20	115	20	20	30	90	180

1343

1344

1345

Table 2. Summary of observation operator state variables.

1346

1347

#	Name	Symbol	Units	Default value	Lower limit	Upper limit
1	Leaf Area Index	LAI	none	0.01	0.01	5.4
2	Canopy height	xh	m	5	1.0	5
3	Leaf radius	xr	m	0.01	0.001	0.1
4	Chlorophyll a,b	C_{ab}	μgcm^{-2}	40	0	200
5	Carotenoids	C_{ar}	μgcm^{-2}	0	0	200
6	Leaf water	C_w	cm^{-1}	0.01	0.00001	0.04
7	Dry matter	C_m	gcm^{-2}	0.01	0.00001	0.02
8	Leaf layers	N	none	1.0	1.0	2.5
9	soil PC 1	s_1	none	0.2	0.05	0.4
10	soil PC 2	s_1	none	0	-0.1	0.1
11	soil PC 3	s_1	none	0	-0.05	0.05
12	soil PC 4	s_1	none	0	-0.03	0.03
13	Leaf angle distribution (categorised)	g	none	uniform	1. planophile 2. erectophile 3. plagiophile 4. extremophile 5. uniform	n/a

1348

1349

1350

1351

Table 3. Transformations applied to approximate linearise state variable response

#	Transformed Symbol	Transformation
1	TLAI	$\exp(-LAI/2.0)$
4	TC_{ab}	$\exp(-C_{ab}/100)$
5	TC_{ar}	$\exp(-C_{ar}/100)$
6	TC_w	$\exp(-50\ C_w)$
7	TC_{dm}	$\exp(-100\ C_{dm})$

1352

1353

Table 4. Upper and lower bounds for the state vector terms (in transformed space, where appropriate) used in the simulations, along with the temporal trajectory assumed.

#	Symbol	Lower limit	Upper limit	Temporal function
1	TLAI	0.067	0.995	$LAI = 0.21 + 3.51 \sin^5(\pi t)$
4	TC_{ab}	0.135	1.0	$C_{ab} = 10.5 + 208.7\, t \; : t <= 0.5$ $C_{ab} = 219.2 - 208.7\, t \; : t >= 0.5$
6	TC_w	0.135	1.0	$C_w = 0.068 +$ $0.020(\sin(\pi t + 0.1) * \sin(6\pi t + 0.1))$
7	TC_{dm}	0.135	1.0	$C_{dm} = 0.01$
8	N	1	2.5	$N = 1$
9	s_1	0.001	0.4	$s_1 = 0.20 + 0.18(\sin(\pi t) * \sin(6\pi t))$

1355
1356
1357
1358

1359

1360

1361

Table 5. Model uncertainty γ for each parameter, calculated from the synthetic model state vector. TC_{dm} and N were kept constant, so have no theoretical model uncertainty associated.

#	Symbol	First difference uncertainty	Second difference uncertainty
1	TLAI	188	8298
4	TC_{ab}	303	7315
6	TC_w	132	2277
9	s_1	212	3861

1362

1363

1364

Table 6: Mean posterior uncertainty. Figures refer to the complete daily time series, while figures in brackets refer to the mean posterior uncertainty only considering the dates where observations are available.

1365

Symbol	Non-cloudy			Cloudy		
	Uncertainty Single Obs.	Uncertainty 1st Diff	Uncertainty 2nd Diff	Uncertainty Single Obs.	Uncertainty 1st Diff	Uncertainty 2nd Diff
TLAI	0.18 (0.05)	0.04 (0.04)	0.06 (0.06)	0.21 (0.05)	0.06 (0.05)	0.09 (0.07)
TC_{ab}	0.20 (0.10)	0.04 (0.04)	0.06 (0.06)	0.22 (0.09)	0.06 (0.05)	0.08 (0.06)
TC_w	0.23 (0.18)	0.07 (0.07)	0.13 (0.13)	0.24 (0.19)	0.10 (0.10)	0.17 (0.16)
TC_{dm}	0.24 (0.22)	0.13 (0.13)	0.28 (0.28)	0.24 (0.23)	0.19 (0.19)	0.36 (0.35)
N	0.29 (0.55)	0.21 (0.21)	0.37 (0.37)	0.27 (0.55)	0.32 (0.32)	0.44 (0.40)
s_1	0.17 (0.04)	0.02 (0.02)	0.03 (0.03)	0.20 (0.04)	0.04 (0.03)	0.05 (0.03)

1366

1367

1368

1369

1370

1371

1372

1373

Table 7: Single observation posterior correlation matrix. Elements above the main diagonal show the results for DoY 186, whereas the elements below the main diagonal represent the median of all dates.

Symbol	TLAI	TC_{ab}	TC_w	TC_{dm}	N	s_1
TLAI	1.00	0.16	-0.05	0.47	-0.25	0.58
TC_{ab}	-0.44	1.00	0.15	-0.11	-0.47	0.34
TC_w	-0.42	0.35	1.00	0.04	0.01	-0.14
TC_{dm}	0.30	0.27	-0.27	1.00	0.42	-0.36
N	0.00	-0.21	0.07	-0.43	1.00	-0.85
s_1	0.76	-0.53	-0.40	-0.25	-0.28	1.00

1374

1375

Table 8: Uncertainty reduction relative to the single observation inversion, as well as percentage of cases where the true parameter lies within the estimated 95% confidence interval. Results for non-cloudy scenario are reported. both complete time series

		Complete time series				Observations only				
#	Symbol	Unc. red 1st diff	Unc. red. 2nd diff	% cases (1st diff)	% cases (2nd diff)	Unc. red 1st diff	Unc. red. 2nd diff	% cases (1st diff)	% cases (2nd diff)	% cases (single)
1	TLAI	4.89	2.96	75.3	90.4	1.44	0.85	72.6	91.8	63.0
4	TC_{ab}	5.24	3.58	61.1	65.2	2.57	1.74	60.3	65.8	65.8
6	TC_w	3.47	1.77	51.2	69.9	2.72	1.38	50.7	71.2	60.3
7	TC_{dm}	1.82	0.85	87.7	100.0	1.64	0.76	87.7	100.0	57.5
8	N	1.40	0.79	59.2	100.0	2.67	1.50	58.9	100.0	60.3
9	s_1	7.59	6.43	67.1	72.3	2.13	1.56	63.0	72.6	75.3
	Mean	4.07	2.73	66.9	83.0	2.20	1.30	65.5	83.6	63.7

1376
1377

Table 9: Uncertainty reduction relative to the single observation, as well as percentage of cases where the true parameter lies within the estimated 95% confidence interval. Results for cloudy scenario.

| #	Symbol	Complete time series				Observations only				
		Unc. red 1st diff	Unc. red. 2nd diff	% cases (1st diff)	% cases (2nd diff)	Unc. red 1st diff	Unc. red. 2nd diff	% cases (1st diff)	% cases (2nd diff)	% cases (single)
1	TLAI	3.33	2.39	82.7	74	0.965	0.68	88.9	91.7	63.9
4	TC_{ab}	3.68	2.93	80.0	89.6	1.82	1.58	61.1	83.3	58.3
6	TC_w	2.33	1.4	64.1	85.2	1.90	1.18	83.3	88.9	61.1
7	TC_{dm}	1.25	0.669	100	100	1.18	0.656	100	100	58.3
8	N	0.835	0.597	91	100	1.73	1.38	88.9	100	58.3
9	s_1	4.65	4.53	63.6	78.1	1.57	1.35	69.4	72.2	75.0
	Mean	2.68	2.09	80.2	87.8	1.53	1.14	82.0	89.3	62.5

Figures

Figure 1. Base level state vector estimated from inverting single observations, (left column) and for model uncertainty unknown and estimated through cross-validation – first difference constraint (central column) and second difference constraint (third column). Results for each of the six parameters are shown in rows. True values are shown as a dashed line. The full lines are the posterior means, and the shaded area represents the associated +/-1.96 standard deviations interval. MSI observations are shown as open symbols. Crosses along the bottom of the third row indicate the location of the cross validation acquisition dates.
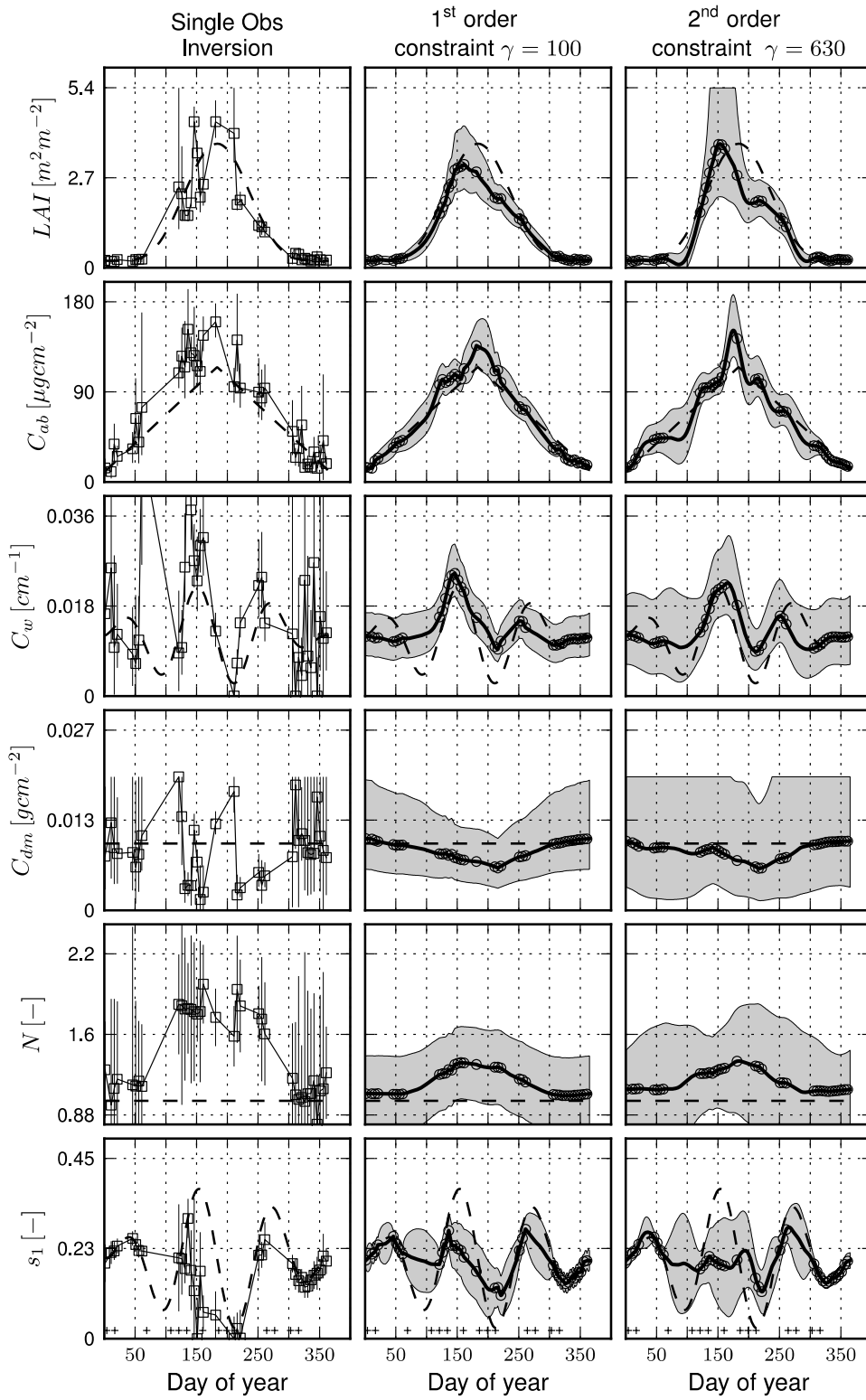
1384

1385

1386
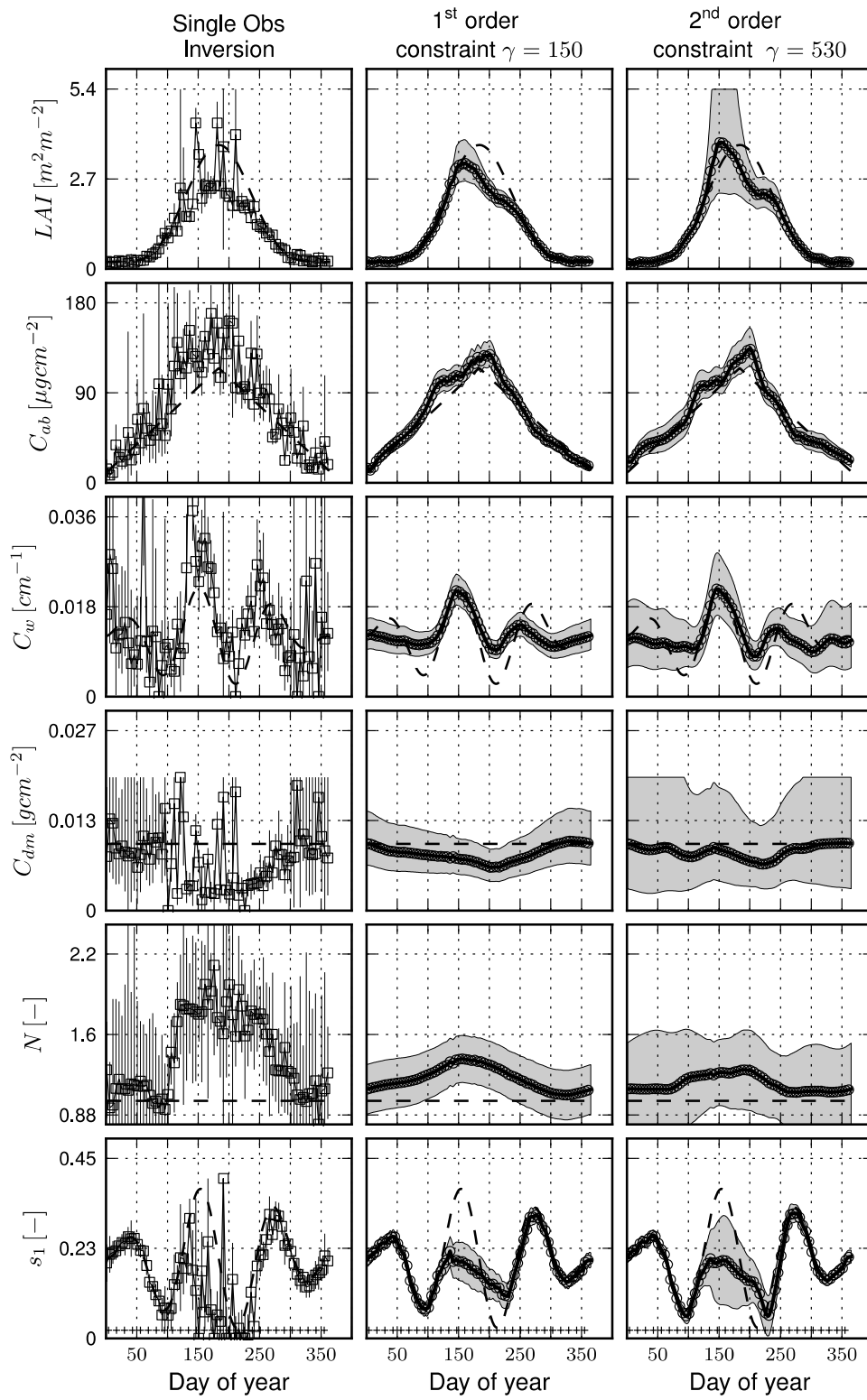
1387 **Figure 2. Error in cross validation scaled by observational uncertainty for varying model**

1388 **uncertainty γ for first and second order constraints. Vertical lines around 200 represent the**

1389 **theoretical value of γ for each of the 4 time-varying state variables using a first order**

1390 **constraint, and vertical lines around 5000 represent the theoretical values for γ for each of the**

1391 **4 time-varying state variables using second order constraint.**
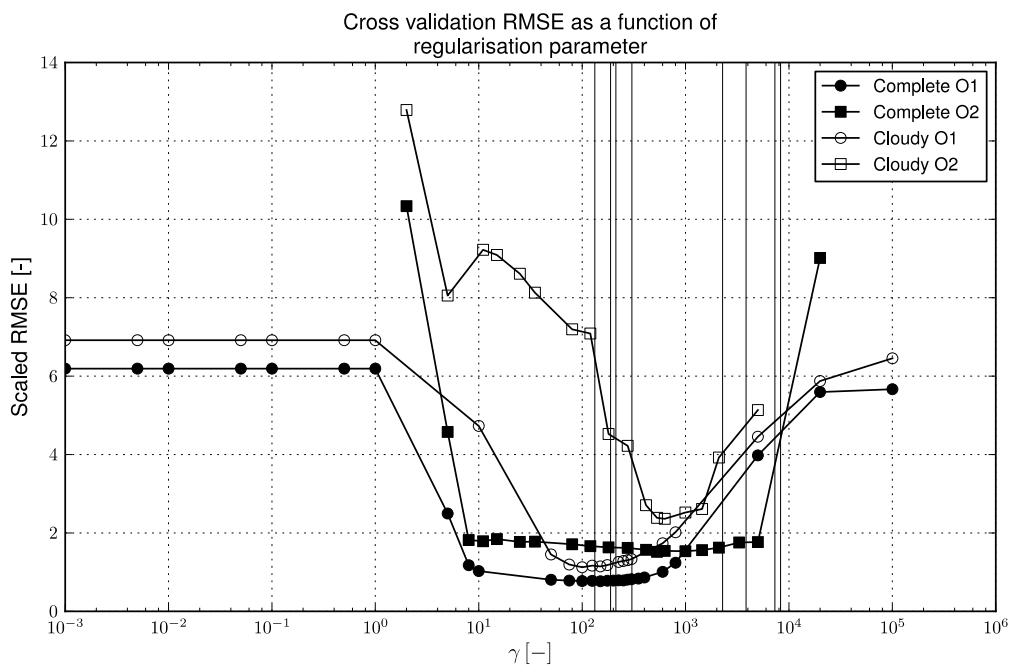
1392

Figure 3. Base level state vector estimated from inverting single observations, (left column) and for model uncertainty unknown and estimated through cross-validation – first difference constraint (central column) and second difference constraint (third column). Reduced number of acquisitions due to cloud cover scenario. Results for each of the six parameters are shown in rows. True values are shown as a dashed line. The full lines are the posterior means, and the shaded area represents the associated +/-1.96 standard deviations interval. MSI observations are shown as open symbols. Crosses along the bottom of the third row indicate the location of the cross validation acquisition dates.
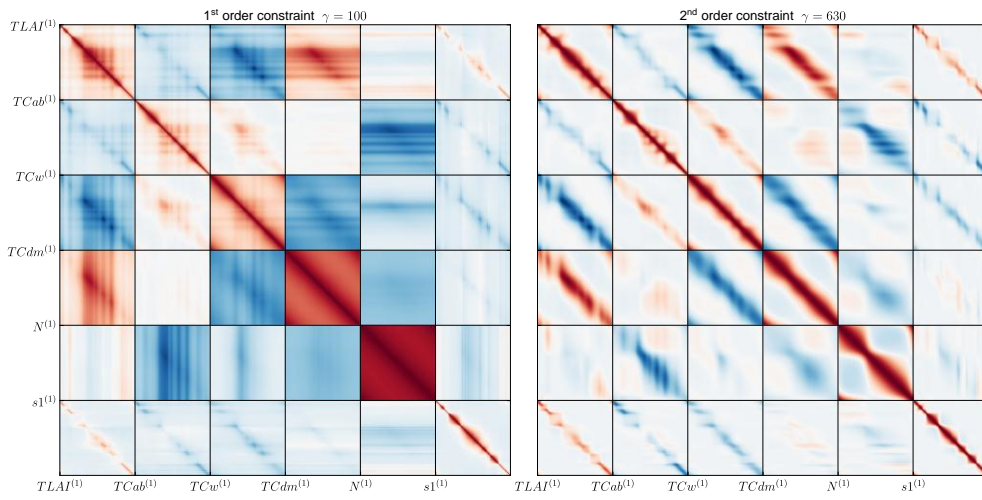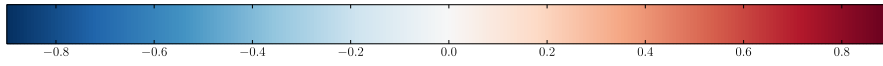
Figure 4. Posterior correlation matrices for the cloudy scenario. Labels indicate the location of the first day for component of the state vector.